NUMERICAL SIMULATION OF HEAT TRANSFER AND STRESS ANALYSIS OF CONTINUOUS CASTING

By

Ali Akbar Iranmanesh

A DISSERTATION

Submitted to
Michigan State University
in partial fulfillment of the requirements
for the degree of

DOCTOR OF PHILOSOPHY

Department of Agricultural Engineering

1981

ABSTRACT

NUMERICAL SIMULATION OF
HEAT TRANSFER AND STRESS ANALYSIS
OF CONTINUOUS CASTING

By

Ali Akbar Iranmanesh

The objective of this study was to use the three-dimensional finite element analysis to predict the temperature and stress distribution in a continuous casting process and provide design engineers with a reliable method of optimizing the location of the bending rolls and radius of the curved portion of continuous casting.

A three-dimensional finite element computer model was developed and used to determine the temperature distribution of the continuous casting and the stress distributions in the straight and curved portions of the casting. Boundary conditions affecting the cooling process, and the stress distribution were varied along the direction of the casting. The material properties were temperature dependent and the latent heat of fusion was incorporated into the specific heat.

The computer results of the temperature distribution compare favorably with the literature. The temperature history and other boundary loads and displacements were

Ali Akbar Iranmanesh

incorporated into an elasticity analysis to determine the stress distribution. The computer results of the stress analysis are presented in a series of graphs showing the ratios of the calculated stress to yield stress at the proper temperature.

The results indicated that the highest stress ratios occur at the bending rolls. The best location of the bending rolls was determined to be as near to the mould as possible. The largest possible radius of curvature is also the most ideal.

Approved_________________________
Major Professor

Approved_________________________
Department Chairman

ACKNOWLEDGMENTS

My sincere appreciation is extended to my major professor, Dr L. J. Segerlind (Agricultural Engineering) for the guidance, suggestions and knowledge he provided me with, as it made this portion of my progam both a pleasing and rewarding experience.

Sincere appreciation is also extended to Dr. M. Kato (Metallurgy, Mechanics and Material Science) for his time and constructive suggestions.

I extend my deepest graditude to my wife for her continual patience, understanding, and encouragement throughout my graduate program.

TABLE OF CONTENTS

Chapter		Page

LIST OF TABLES

LIST OF FIGURES

Figure		Page

I. INTRODUCTION, LITERATURE REVIEW, AND OBJECTIVES

1.1 Introduction

The production of an ingot in a length many times longer than the mould in which it is formed is known as continuous casting. Figure 1-1 shows the estimated tonnage of steel continuously cast worldwide between 1950 and 1972. The rapid growth rate in the late sixties came about with the use of a caster that was designed to meet the semifinished steel needs of modern production facilities utilizing the output of the basic oxygen and electric furnace shops. The process now occupies an important place in the metallurgical industry and the entire world of the metal user. The proportion of the world steel production that is continuously cast will continue to rise because many of the new plants being designed or constructed use continuous casting as their source of semifinished product.

In all continuously cast installations, molten metal is poured into a water cooled mould in which the metal starts to solidify. Rolls below the mould withdraw the solidified metal at a constant velocity. An outer skin of solidified metal is formed within the mould. This tendency of solidification, however, is counteracted by the pressure of the molten core until the solidified metal is thick enough to support this pressure. At this stage the solidified metal separates from the mould walls and the mould is no longer necessary. The metal can be cooled directly by water sprays or by immersion in a water bath. A schematic diagram of a continuous casting installation is shown in Figure 1-2.

Continuous casting differs significantly from static casting. If minor fluctuations due to the reciprocating motion of the mould are neglected, the temperature field within a continuous casting installation is constant in time. This is not so in static casting. In the latter case, heat lost by the metal heats the material of the mould, and the mould has to be included in the analysis. In continuous casting, however, the temperature of the mould is steady in time, and thus the boundary conditions at the metal-mould interface involve the heat flux but not the temperature.

The rate of heat extraction and solidification in conventional casting is relatively slow. The solidification time is measured in hours as compared to minutes for continuous casting. The statically cast ingot experiences a single cooling environment over its solifification period. The continuously cast section encounters three entirely different cooling environments - mould, spray, and radiation - before fully solidifying. As a result, the continuously cast section is subjected to much steeper temperature gradients which can change rapidly from one zone to the next. As a consequence, thermal stresses are a more serious problem in the continuously cast ingot.

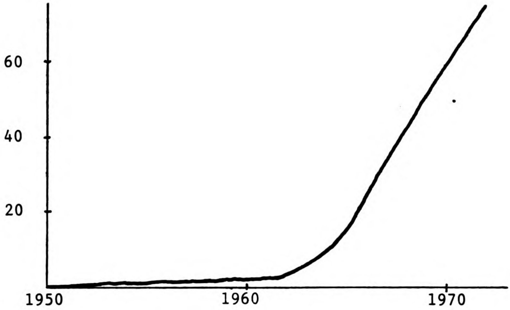

FIGURE 1.1 World wide annual continuous casting capacity
Lankford 1972

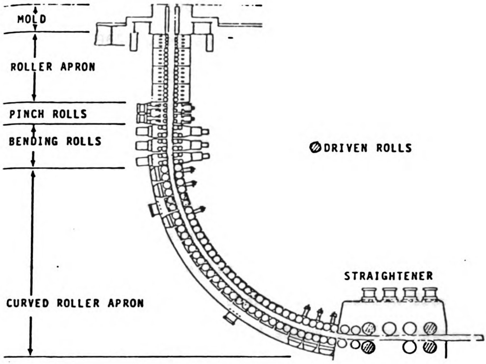

FIGURE 1.2 Section view through continuous caster
Richards 1971

The conventionally cast ingot is not stressed by pinch rolls or bending and straightening operations during the solidification process. The continuously cast ingot does experience these loads.

Because of the popularity of the continuous casting process, there is a need to understand the thermal behavior and the nature of the thermal stresses, especially as these two quantities combine to produce crack formations within the continuously cast ingot.

1.2 Literature Review

Continuous casting of the metals existed before 1950 but the most important theoretical and experimental work has been published since 1965.

Hills (1965) used an integral profile technique to solve the heat transfer equations in terms of the heat transfer coefficient in the mould. One of his equations relates the heat removed by the mould cooling water to the heat transfer coefficient, and thus enables this coefficient to be determined from a heat balance on the mould cooling water. The general results reported were that the variation of the heat transfer coefficient with dwell time in any particular mould is much less than its variation from mould to mould. The effect of the mould shape and its operational conditions are very significant.

Mizikar (1970) measured an experimental value of heat transfer coefficient of the spray cooling water by using

different nozzle shapes, varying the distance between the sprayer and the ingot, the rate of application of the cooling water, the angle of the nozzle to spray, and the droplet size of the water spray. The result was a series of graphs which can be used to design the spray cooling process.

Morton (1973) added radioactive gold to the liquid pool during the continuous casting of mild steel. From autoradiographs of billet sections, the pool profile and the extent of liquid mixing in the pool were established. The results clearly indicated the position of the solid liquid interface in the mould region.

Koler et al. (1973) developed a mathematical model for large ingot solidification. They emphasized some technical difficulties related to computation of the heat of fusion. The "C_p" method which had been used in the past (Marrone et al., 1970) was used to obtain the effective specific heat. The result was reported to be at least as good as any other method.

Lait et al. (1974) used a one-dimensional finite difference model to calculate the temperature field and pool profiles of continuously cast steel. They examined two different surface boundary conditions for the mould region; a constant mould heat transfer coefficient, and an empirical heat flow relationship. The results obtained were reported to be in reasonable agreement with experimental results for low carbon billets over most of the mould region.

Den Hartog et al. (1975) developed a two-dimensional finite difference model of ingot solidification, taking special care to incorporate the real physics of the solidification process within the mould. Application of the derived relationship between solidification time and internal quality of the ingot, together with the criterion for good rollability which was discussed in their paper, allowed the determination of the required cooling and reheating times of ingots of different sizes.

Mathew and Brody (1976) used a two-dimensional axisymmetric finite element model to simulate the solidification of a cylindrical alloy ingot. This was the first work which took into account both radial and axial heat conduction. The result reported to agree very well with the experimental results reported by Morton (1970).

The development of internal and surface cracks is an important problem in continuous casting.

Grill et al. (1976) used a two-dimensional finite element analysis to numerically calculate the stresses in continuous casting of steel. Their goal was to assist in the optimization of casting conditions to avoid crack formation. They calculated an approximation of the location of halfway cracks which may occur in the solid near the solidification front.

Schmidt and Fredriksson (1975) investigated the formation of macrosegregation and center line cracks. Center line cracks occur when the last liquid solidifies in the center of the ingot. They concluded that the solidification sequence determines the macrosegregation pattern. Different cooling conditions were applied in the secondary cooling zone of a billet cast machine to reduce the center line cracks and macrosegregation.

1-3 Objectives

A review of the literature indicates that there does not exist a study which calculates the three-dimensional temperature field for a continuously cast ingot and there is no information whatsoever (to the best of the author's knowledge) about the stresses in the curved portion of the ingot. Items such as where the bending rolls shoud be located, what should be the radius of the curvature, and the stresses within the curved portion of casting ingot have not been studied.

The objectives of this work were:

1. Develop a three-dimensional finite element model of the heat transfer process in a continuously cast ingot.
2. To develop a three-dimensional finite element elasticity program to calculate the stress field within the vertical section and within the curved portion of a continuously cast ingot.

II. THEORY OF HEAT TRANSFER

2.1 Governing Equation

The thermal aspects of solidification are complex because they involve several parameters. The temperature dependent thermal properties of solidifying metal, the latent heat release due to the solidification, the thermal properties of the mould material, the mould geometry, the progress of the solidification front with time, the air-gap formation within the mould, the pouring temperature, and the speed of casting are a few of the parameters involved.

The differential equation of heat flow expressed in rectangular coordinates (x,y, z) and referenced to a fixed origin in the solid has the well known form

$$(2\text{-}1) \qquad \frac{\partial}{\partial x}(K_{xx}\frac{\partial T}{\partial x}) + \frac{\partial}{\partial y}(K_{yy}\frac{\partial T}{\partial y}) + \frac{\partial}{\partial t}(K_{zz}\frac{\partial T}{\partial z}) = PC_p\frac{\partial T}{\partial t}$$

where T is temperature (^{o}K) and it is a function of x, y, z (the fixed coordinates) and t (time, seconds). The coefficients K_{xx}, K_{yy}, and K_{zz} are the thermal conductivity (watts/cm - ^{o}K) in x, y, and z directions, respectively. Also, C_p is the specific heat (J/g - ^{o}K) and P is density (g/cm^3).

D. Rosenthal (1946) developed the mathematical equation for a moving heat source which is applicable to the continuous casting process. The heat source is moving with respect to an origin which is fixed on the casting. If there is another coordinate system which is moving with respect to the fixed coordinate system with a constant velocity U_c (cm/sec), then the temperature in the new origin will be defined as $T = f(\xi, \eta, \zeta, t')$, where ξ, η, ζ are moving coordinates and t' is time measured in this coordinate (Figure 2-1). Considering the (x,y,z) coordinates fixed on the top of the mould, where the alloy is liquid and (ξ, η, ζ) coordinates are fixed on the cast ingot and the direction of casting is z or ζ (Figure 2-1).

For a moving coordinate

$$z - \zeta = U_c t \quad \text{or} \quad \zeta = z - U_c t$$

and
$$\frac{\partial \zeta}{\partial z} = 1, \quad \frac{\partial \zeta}{\partial t} = -U_c, \quad \frac{\partial t'}{\partial t} = 1$$

so
$$\frac{\partial T}{\partial t} = \frac{\partial T}{\partial \zeta} \cdot \frac{\partial \zeta}{\partial t} + \frac{\partial T}{\partial t'} \cdot \frac{\partial t'}{\partial t}$$

or
$$\frac{\partial T}{\partial t} = -U_c \frac{\partial T}{\partial \zeta} + \frac{\partial T}{\partial t'}$$

and also
$$\frac{\partial T}{\partial x} = \frac{\partial T}{\partial \xi}, \quad \frac{\partial T}{\partial y} = \frac{\partial T}{\partial \eta}, \quad \text{and} \quad \frac{\partial T}{\partial z} = \frac{\partial T}{\partial \zeta}$$

After substitution into equation 2-1

$$\text{(2-2)} \quad \frac{\partial}{\partial \xi}\left(K_{xx} \frac{\partial T}{\partial \xi}\right) + \frac{\partial}{\partial \eta}\left(K_{yy} \frac{\partial T}{\partial \eta}\right) + \frac{\partial}{\partial \zeta}\left(K_{zz} \frac{\partial T}{\partial \zeta}\right) = PC_p\left(\frac{\partial T}{\partial t'} - U_c \frac{\partial T}{\partial \zeta}\right)$$

or in the general form

$$\nabla(K \nabla T) = -U_c PC_p \frac{\partial T}{\partial \zeta} + PC_p \frac{\partial T}{\partial t'}$$

In a quasi stationary state $\frac{\partial T}{\partial t'} = 0$. Changing the notation yields the governing equation

$$\text{(2-3)} \quad \frac{\partial}{\partial x}\left(K_{xx} \frac{\partial T}{\partial x}\right) + \frac{\partial}{\partial y}\left(K_{yy} \frac{\partial T}{\partial y}\right) + \frac{\partial}{\partial z}\left(K_{zz} \frac{\partial T}{\partial z}\right) + U_c PC_p \frac{\partial T}{\partial z} = 0$$

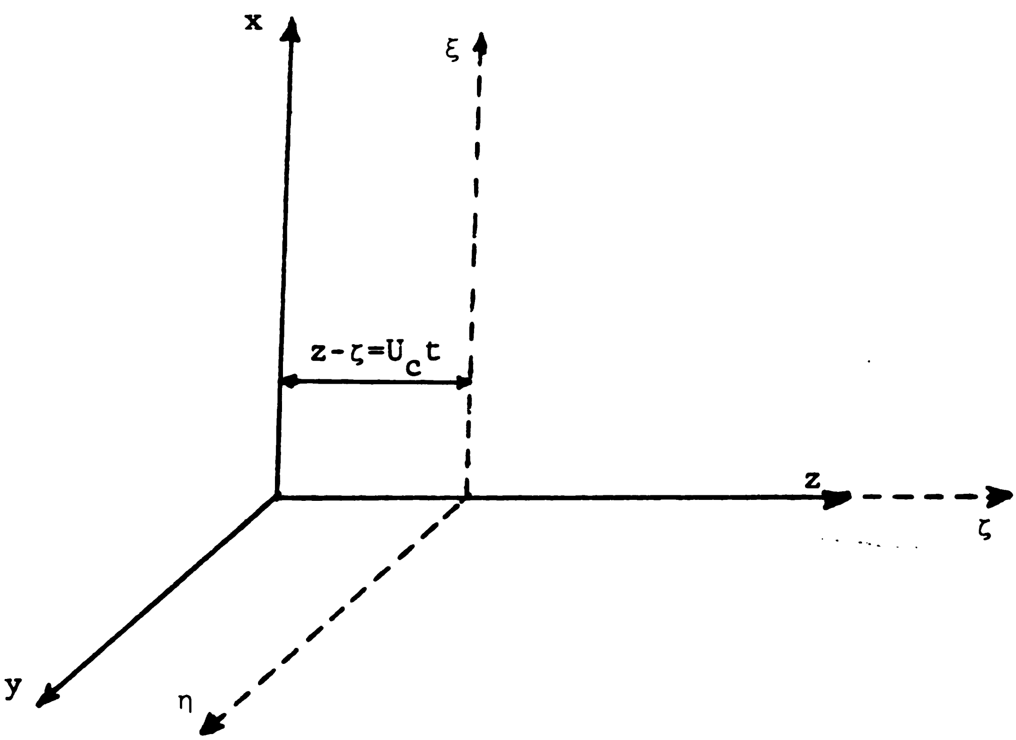

Figure 2-1· Relation of fixed and moving coordinates.

2-2 Boundary Conditions

Three different types of boundary conditions occur when the equation 2-3 is applied to a continuous casting ingot. These are shown in Figure 2-2. At time zero the temperature profile of the slice at meniscus is equal to the incoming metal temperature. The center surface boundary conditions

$$\frac{\partial T}{\partial x} = 0 \qquad \text{and} \qquad \frac{\partial T}{\partial y} = 0 \tag{2-4}$$

are the result of the assumption of symmetrical heat transfer from all edges of the casting. The surface boundary condition

$$q_{out} = f(t) \tag{2-5}$$

was varied as indicated in Figure 2-2 to represent the three types of cooling: mould, spray and radiation.

The first zone of cooling is in the mould. Heat transfer in the mould is governed by a series of three resistances, the casting-mould interface, the mould wall, and the mould-cooling water interface. The thermal resistance of the mould wall and mould cooling water interface are usually quite small (Hill, 1965) compared with the thermal resistance between the casting and the mould, which consequently controls the rate of heat transfer in the mould. As shown in Figure 2-3 it is generally accepted that the casting-mould interface can be divided into three sections: 1) from the meniscus to the point where the

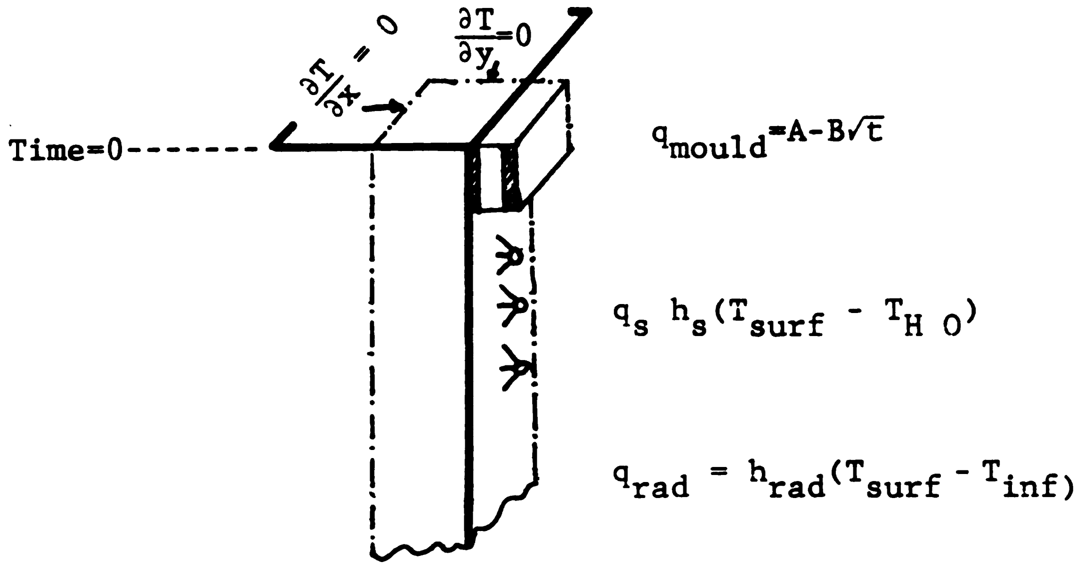

Figure 2-2 Heat transfer boundary conditions.

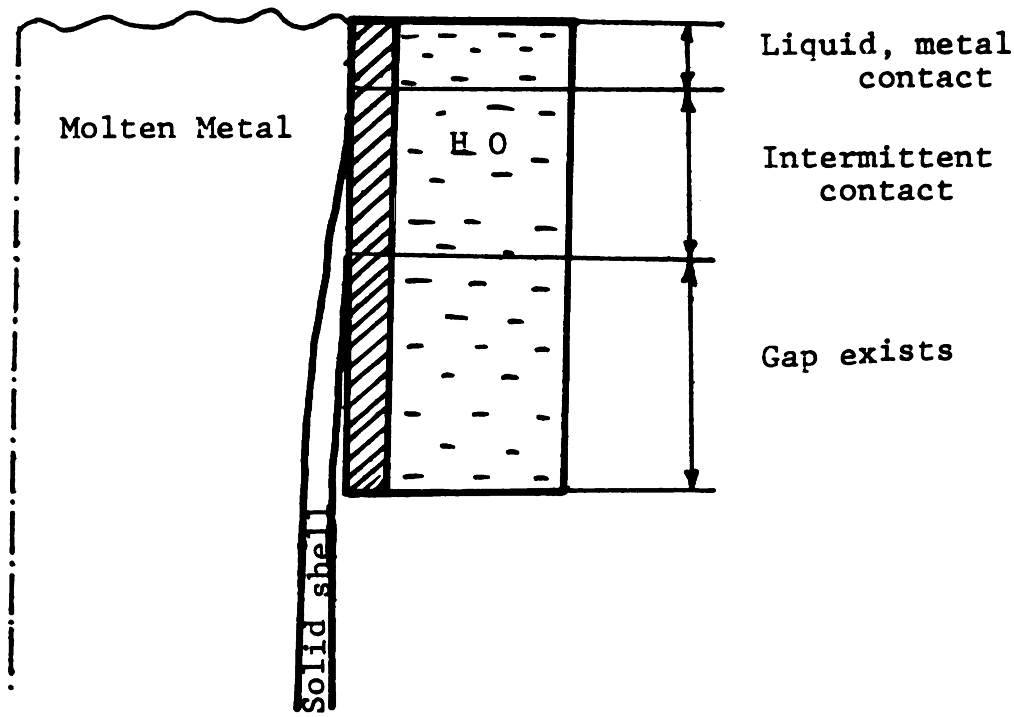

Figure 2-3 Mould conditions.

shell begins to form. In this region, liquid metal is separated from the mould by a thin layer of lubricating material; 2) the region over which the shell has insufficient strength to pull away from the mould, but due to the condition of the casting surface intermittent contact exists; and 3) the zone over which a definite gap exists. Heat transfer takes place by radiation and conduction through the gas in the gap.

Considering the combination of the first and second zones as a zone having good contact and the third zone as an air gap, Mathew (1976) developed the following model. In the zone of good contact, the total resistance to the heat flow (U_{good}) is the sum of the resistances due to a thin film of oil between the mould and the casting (U_{oil}), the thickness of the mould wall (X_{mould}), and the interface between the mould and mould cooling water. His result was

$$(2\text{-}6) \qquad U_{good} = U_{oil} + \frac{X_{mould}}{K_{mould}} + \frac{1}{h_{water}}$$

where K_{mould} is the conductivity of the mould materials, and h_{water} is the heat transfer coefficient at the mould-water interface. In the zone where the gap exists, the thermal resistance from the shell surface to the mould cooling water is given by:

$$(2\text{-}7) \qquad U_{gap} = \frac{1}{\frac{K_{gap}}{\Delta g_{gap}} + \sigma_s \varepsilon_e (T^4 - T_m{}^4)} + U_{good}$$

where U_{gap} is the total thermal resistance from the skin surface to the mould cooling water, K_{gap} and g_{gap} are the conductivity and the thickness of the gap, respectively; T and T_m are the casting surface temperature and the mould surface temperature. Also, σ_s is the Stefan Boltzman constant (5.672×10^{-12} watt/cm^2 - $^0K^4$) and ε_e is the emissivity (0.3).

The heat flux from solidifying steel to the mould cooling water has been measured by Savage and Pritchared (1954) in an experimental continuous casting mould as a function of time. They developed the equation

$$q = 640 - 80\sqrt{t} \qquad (2\text{-}8)$$

to describe the process. In equation 2-8, q is the flux of heat from the casting face to the mould cooling water and t is the time for which the material is in contact with the mould.

Cooling of the ingot once it has left the mould consists of one or several stages of spray, and heat loss by radiation. The heat transfer coefficient for the spray boundary was determined experimentally by Mizikar (1970). It can be modeled as

$$q_s = h_s(T - T_w) \qquad (2\text{-}9)$$

where h_s is the spray heat transfer coefficient (watt/cm^2- ^0K) , T is the casting surface temperature and T_w is the spray cooling water temperature. The heat transfer in the radiation cooling is given by

$$q = h_{rad}(T - T_{inf}) \tag{2-10}$$

where the effective heat transfer coefficient h_{rad} is given by

$$h_{rad} = \sigma_s \varepsilon_e (T + T_{INF})(T + T_{INF}) \tag{2-11}$$

T is the casting surface temperature and T_{INF} is the surrounding temperature.

2.3 Latent Heat and Material Properties

Heat conduction in continuous casting must include the change of phase. During the solidification process there exists a solid surface and a liquid surface and a transition zone between these where latent heat is being absorbed. A number of methods of handling the latent heat in a solidifying ingot were studied. Some of the various approaches to this problem are outlined below.

In Campagna's dissertation (1970), an equation for the liquid-solid interface was derived and the latent heat of fusion was included as a function of the fraction solidified. The use of Campagna's technique in a numerical solution requires very small elements and thus lots of computer memory and computation time. Hence, this method was not employed.

In a Japanese study, Chihara an Usui (1967), a transformation was performed on the heat equation so calculations could be done using enthalpy instead of temperature. This allowed the latent heat of fusion to be added to the enthalpy whenever a unit had solidified. This was only an approximation and there appeared to be no particular advantage in using it. An attempt was made by Fischer (1970) to include the latent heat of fusion as additional super heat using the relation $\Delta T = L/C$, C being the average specific heat, ΔT being the additional super heat, and L the latent heat. This was a very rough approximation and produced poor results.

After considering various other approaches it was decided to use a method termed the "C_p method" which is presented by Koler et al. (1973). In this method the latent heat of fusion is added to the specific heat over some predetermined temperature range. The calculations are made with what can be called an "effective specific heat" instead of actual specific heat. This allows one to calculate directly from the heat equation and no special treatment at the solidification front is required. The problem with this approach is the determination of a C_p function across the mushy zone, so that the heat released represents in a realistic fashion what actually happens in the transition zone. Once the C_p function is determined, the computations present no particular difficulty. Another advantage of the C_p method is that it is easily incorporated in a three-dimensional model.

The specific heat was modified to take into account the release of latent heat of fusion in the transition zone of the ingot during solidification (Koler et al., 1973).

The specific heat before and after modification are shown in Figures 2-4a and 2-4b.

A modification of thermal conductivity at temperatures above that of liquidification was also made to take into account the effect of convection currents in the molten core of the ingot. The value of thermal conductivity of molten steel was multiplied by a factor of ten (Fischer, 1965). The variation of thermal conductivity from room temperature to the steel making temperature is shown in Figure 2-4c.

2-4 Finite Element Formulation

The finite element method has been applied to almost every area of engineering in the last 20 years. It is a numerical procedure for solving differential equations which a) utilize an integral formulation of the problem and b) use continuous piece wise smooth functions(s) to approximate the unknown parameters. The finite element method like other numerical methods is based on the assumption that a continuous body can be divided into a number of discrete elements, each having its own set of thermal and mechanical properties.

By assuming $K_{xx} = K_{yy} = K_{zz} = K$, the governing differential equation reduces to

$$\frac{\partial}{\partial x}\left(K\frac{\partial T}{\partial x}\right) + \frac{\partial}{\partial y}\left(K\frac{\partial T}{\partial y}\right) + \frac{\partial}{\partial z}\left(K\frac{\partial T}{\partial z}\right) + U_C P C_p \frac{\partial T}{\partial z} = 0 \qquad (2\text{-}12)$$

with the boundary conditions 2-8 through 2-11. The finite

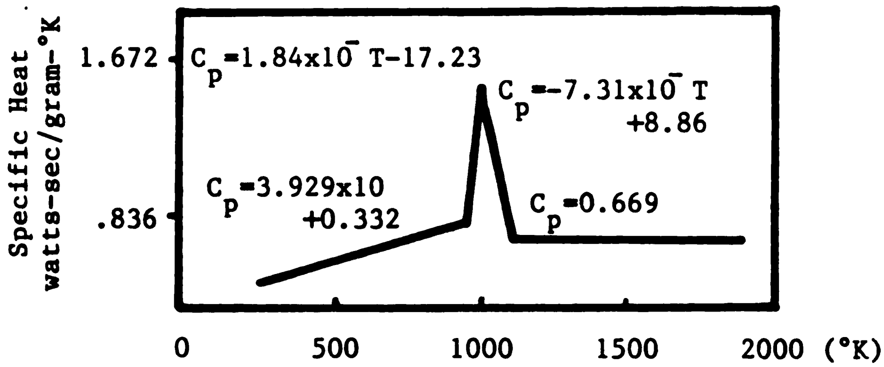

Figure 2-4a Specific heat (C_p) profile.

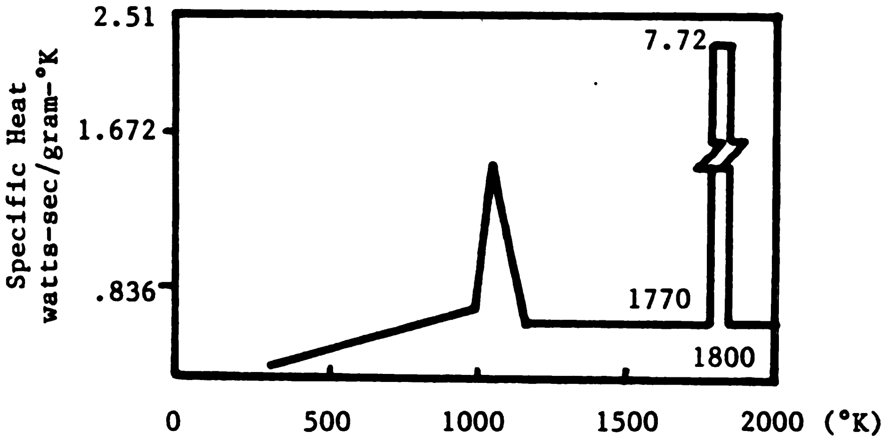

Figure 2-4b Specific heat (C_p) after modification. Rammerstorfer 1979

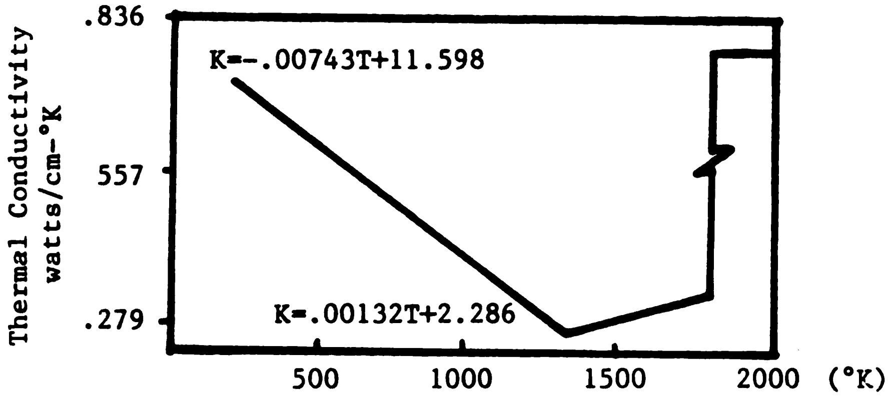

Figure 2-4c Thermal conductivity profile. Krutz 1975

element equations can be obtained using a variational approach or Galerkin's method. The element stiffness matrix [ESM] is given by Segerlind (1976) as

(2-13) $$[ESM]^{(e)} = \int_{v^{(e)}} [B^{(e)}]^T [D^{(e)}][B^{(e)}]dv + \int_{v^{(e)}} U_c P^{(e)} C_p^{(e)} [N^{(e)}]^T \frac{\partial N^{(e)}}{\partial z} dv + \int_{s^{(e)}} h^{(e)} [N^{(e)}]^T [N^{(e)}]ds$$

and the element force vector $\{EF\}$ is

(2-14) $$\{EF\} = \int_{s^{(e)}} hT_{inf} [N^{(e)}]^T ds$$

where

$$[D] = K \begin{bmatrix} 1 & 0 & 0 \\ 0 & 1 & 0 \\ 0 & 0 & 1 \end{bmatrix}$$

[N] is a matrix involving the shape functions, and [B] is a matrix related to the derivatives of the shape functions. A twenty node prism element was used in this study. The matrices [N] and [B] were

$$[N] = [N_1 \ N_2 \ N_3 \ . \ . \ . \ . \ . \ . \ . \ . \ . \ N_{20}]_{1x20}$$

$$[B] = \begin{bmatrix} \partial N_1/\partial x & \partial N_2/\partial x & \partial N_3/\partial x. \ . \ . \ . \ . \ . \partial N_{20}/\partial x \\ \partial N_1/\partial y & \partial N_2/\partial y & \partial N_3/\partial y. \ . \ . \ . \ . \ . \partial N_{20}/\partial y \\ \partial N_1/\partial z & \partial N_2/\partial z & \partial N_3/\partial z. \ . \ . \ . \ . \ . \partial N_{20}/\partial z \end{bmatrix}_{3x20}$$

The coefficient h in equations 2-13 and 2-14 is the heat transfer coefficient for the spray boundary condition or the radiation boundary condition. The shape functions for the twenty node prism element used in this study are given in a general form by Zienkiewicz (1978). The explicit equations are given in Table 2.1. The location of the element nodes are as shown in Figure 2-5.

The integrals in equations 2-13 and 2-14 were evaluated numerically using a Gauss-Legendre technique (Segerlind, 1976). The numerical integration requires a change of variables from the (x,y,z) coordinate system to a natural coordinate system (ξ,η,ζ), where each variable varies between -1 and +1. The location of these two coordinates is shown in Figure 2-6. The change in variable relationship is

(a) $$dv = dxdydz = |\det[J]|\,d\xi d\eta d\zeta$$

Segerlind (1976), where [J] is the Jacobian matrix of the transformation.

(b) $$[J] = \begin{bmatrix} \partial x/\partial\xi & \partial y/\partial\xi & \partial z/\partial\xi \\ \partial x/\partial\eta & \partial y/\partial\eta & \partial z/\partial\eta \\ \partial x/\partial\zeta & \partial y/\partial\zeta & \partial z/\partial\zeta \end{bmatrix}$$

Table 2-1 The shape function for the twenty nodes prism element.

$N_1 = 1/8(\xi-1)(1-\eta)(1-\zeta)(\xi+\eta+\zeta+2)$

$N_2 = 1/4(1-\xi^2)(1-\eta)(1-\zeta)$

$N_3 = 1/8(1+\xi)(1-\eta)(1-\zeta)(\xi-\eta-\zeta-2)$

$N_4 = 1/4(1-\eta^2)(1+\xi)(1-\zeta)$

$N_5 = 1/8(1+\xi)(1+\eta)(1-\zeta)(\xi+\eta-\zeta-2)$

$N_6 = 1/4(1-\xi^2)(1+\eta)(1-\zeta)$

$N_7 = 1/8(1-\xi)(1+\eta)(1-\zeta)(\eta-\xi-\zeta-2)$

$N_8 = 1/4(1-\eta^2)(1-\xi)(1-\zeta)$

$N_9 = 1/4(1-\zeta^2)(1-\xi)(1-\eta)$

$N_{10} = 1/4(1-\zeta^2)(1+\xi)(1-\eta)$

$N_{11} = 1/4(1-\zeta^2)(1+\xi)(1+\eta)$

$N_{12} = 1/4(1-\zeta^2)(1-\xi)(1+\eta)$

$N_{13} = 1/8(1-\xi)(1-\eta)(1+\zeta)(\zeta-\xi-\eta-2)$

$N_{14} = 1/4(1-\xi^2)(1-\eta)(1+\zeta)$

$N_{15} = 1/8(1+\xi)(1-\eta)(1+\zeta)(\xi-\eta+\zeta-2)$

$N_{16} = 1/4(1-\eta^2)(1+\zeta)(1+\xi)$

$N_{17} = 1/8(1-\xi^2)(1+\eta)(1+\zeta)(\xi+\eta+\zeta-2)$

$N_{18} = 1/4(1-\xi^2)(1+\eta)(1+\zeta)$

$N_{19} = 1/8\ (1-\xi)(1+\eta)(1+\zeta)(\eta+\zeta-\xi-2)$

$N_{20} = (1-\eta^2)(1-\xi)(1+\zeta)$

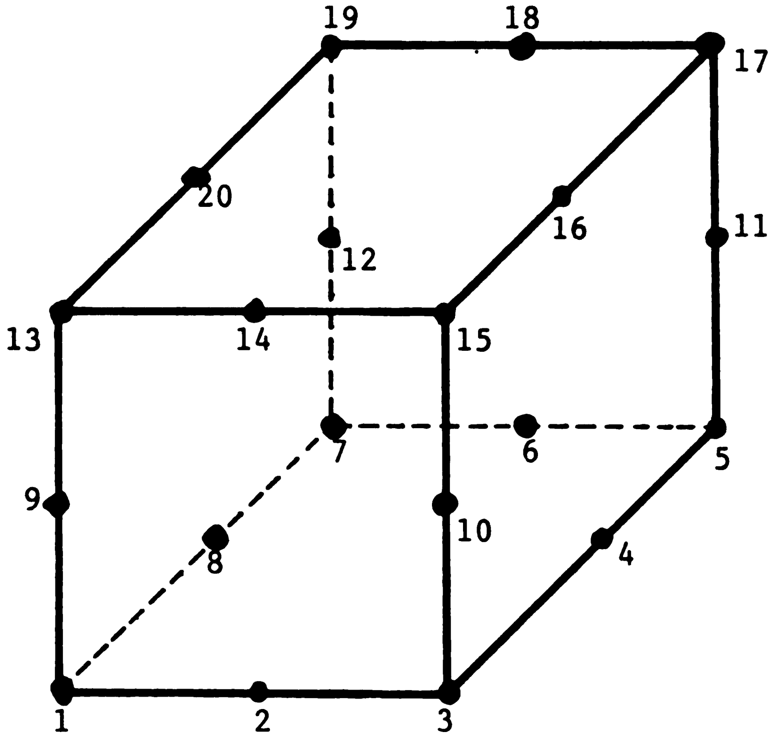

Figure 2-5 Location of the twenty nodes.

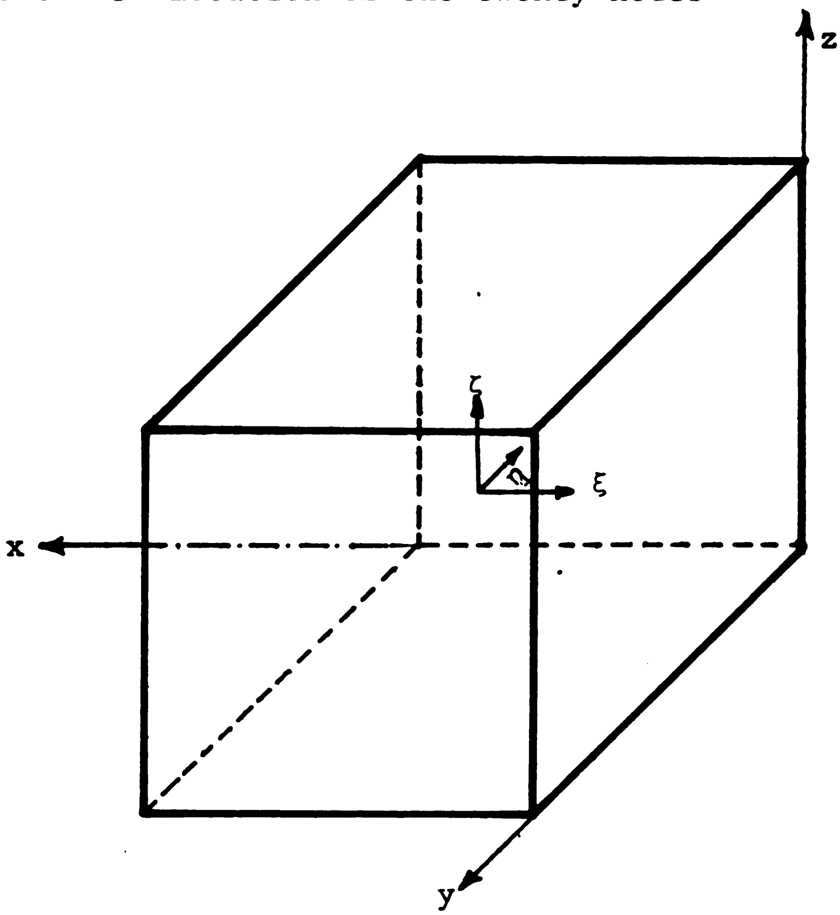

Figure 2-6 Location of natural and cartesion coordinates.

Also

$$\frac{\partial N_i}{\partial \xi} = \frac{\partial N_i}{\partial x} \cdot \frac{\partial x}{\partial \xi} + \frac{\partial N_i}{\partial y} \cdot \frac{\partial y}{\partial \xi} + \frac{\partial N_i}{\partial z} \cdot \frac{\partial z}{\partial \xi}$$

(c)
$$\frac{\partial N_i}{\partial \eta} = \frac{\partial N_i}{\partial x} \cdot \frac{\partial x}{\partial \eta} + \frac{\partial N_i}{\partial y} \cdot \frac{\partial y}{\partial \eta} + \frac{\partial N_i}{\partial z} \cdot \frac{\partial z}{\partial \eta}$$

$$\frac{\partial N_i}{\partial \zeta} = \frac{\partial N_i}{\partial x} \cdot \frac{\partial x}{\partial \zeta} + \frac{\partial N_i}{\partial y} \cdot \frac{\partial y}{\partial \zeta} + \frac{\partial N_i}{\partial z} \cdot \frac{\partial z}{\partial \zeta}$$

so each column of [B] is given by

(d)
$$[B(\xi,\eta,\zeta)] = \begin{bmatrix} \partial N_i/\partial x \\ \partial N_i/\partial y \\ \partial N_i/\partial z \end{bmatrix} = [J]^{-1} \begin{bmatrix} \partial N_i(\xi,\eta,\zeta)/\partial \xi \\ \partial N_i(\xi,\eta,\zeta)/\partial \eta \\ \partial N_i(\xi,\eta,\zeta)/\partial \zeta \end{bmatrix}$$

Substituting a, b, c and d into equation 2-13 and 2-14 produces

(2-15)
$$\begin{aligned}[ESM] = &\int_{-1}^{1}\int_{-1}^{1}\int_{-1}^{1} [B(\xi,\eta,\zeta)]^T[D][B(\xi,\eta,\zeta)]\,|\det[J]|\,d\xi d\eta d\zeta \\ &+ \int_{-1}^{1}\int_{-1}^{1}\int_{-1}^{1} U_c C_p P[N(\xi,\eta,\zeta)]^T \frac{\partial N_i}{\partial \zeta}\,|\det[J]|\,d\xi d\eta d\zeta \\ &+ \int_{-1}^{1}\int_{-1}^{1} h[N(\xi,\eta)]^T[N(\xi,\eta)]\,|\det[J]|\,d\xi d\eta\end{aligned}$$

Twenty seven integration points are required to numerically integrate the volume integral (2-15)(Segerlind, 1976). Table 2-2 gives the location of these integration points along with their weighing coefficient. The integration form of 2-15 is:

$$[ESM] = \sum_{i=1}^{3} \sum_{J=1}^{3} \sum_{k=1}^{3} \left[f_1(\xi_i, \eta_J, \zeta_k) H_{iJk} + U_c C_p P f_2(\xi_i, \eta_J, \zeta_k) H_{iJk}\right]$$

(2-16)

$$\cdot \det[J] \quad + \sum_{i=1}^{3} \sum_{J=1}^{3} \left[f_3(\eta_J, \zeta_k) H_{Jk}\right] \det[J]$$

where

$$f_1(\xi_i, \eta_J, \zeta_k) = [B]^T [D][B]$$

$$f_2(\xi_i, \eta_J, \zeta_k) = U_c P C_p [N]^T \frac{\partial N}{\partial \zeta}$$

$$f_3(\xi_i, \eta_J) = h[N]^T [N]$$

and H_{iJk} from table 2-2 are W's.

(2-17) $$\{EF\} = \int_{-1}^{1}\int_{-1}^{1} h T_{inf} [N(\xi,\eta)]^T |\det[J]| d\xi d\eta$$

The element matrices contain a surface integral

$$ds = dxdy = |\det[J]| d\xi d\eta$$

and when integration is on the surface either ξ, η or ζ will be constant and equal to ± 1. If for example $\xi = \pm 1$ so the derivatives of ξ with respect to x, y and z are zeroes. The Jacobian matrix takes on the following form

Table 2-2 Distance of the sampling points to the center of natural coordinates.
$A = 0.774597$, $B = 8/9$ and $C = 5/9$

ξ	η	ζ	W
0	0	0	B^3
		$\pm A$	B^2C
0	+A	0	B^2C
		$\pm A$	BC^2
0	-A	0	B^2C
		$\pm A$	BC^2
+A	0	0	B^2C
		$\pm A$	BC^2
+A	+A	0	BC^2
		$\pm A$	C^3
$\pm A$	-A	0	BC^2
		$\pm A$	C^3
-A	0	0	B^2C
		$\pm A$	BC^2
-A	+A	0	BC^2
		$\pm A$	C^3
-A	-A	0	BC^2
		$\pm A$	C^3

$$[J_s]_{\text{on S at } \xi = \pm 1} = \begin{bmatrix} 1 & 0 & 0 \\ \partial x/\partial\eta & \partial y/\partial\eta & \partial z/\partial\eta \\ \partial x/\partial\zeta & \partial y/\partial\zeta & \partial z/\partial\zeta \end{bmatrix}$$

The unit value on the diagonal eliminates the singularity of the Jacobian, so that an inverse can be obtained. The numerical integration form of 2-16 is

$$(2\text{-}18) \qquad \{EF\} = \sum_{i=1}^{3} \sum_{J=1}^{3} \left[f_4(\pm 1, \eta_i, \zeta_s) H_{iJ} \right] |\det[J_s]|$$

where $$f_4(\pm 1, \eta_i, \zeta_s) = hT_{inf}[N]^T$$

The last integral of [ESM] is also a surface integral and the same procedure is used to evaluate it. Surface integrals were evaluated only for those elements which have the spray or radiation boundary condition.

The temperature at any given point in an element can be calculated using

$$T = \sum_{i=1}^{20} T_i N_i$$

where T_i is the nodal temperature and N_i is the shape function for a given element evaluated at the point for which the temperature is needed. This equation was used to evaluate the temperature at the integration point for determining the material properties.

t

i

h

o

c:

III. STRESS ANALYSIS OF THE CONTINUOUS CASTING PROCESS

3-1 General

During the continuous casting of steel, high stresses develop in the solidifying shell. The stress arise from a number of different forces acting externally and internally on the casting. Internal forces can be generated by expension or contraction of the shell resulting from a sudden change in temperature. For example, rapid reheating of the surface can occur immediately below the mould or spray zones and cause tensile stresses to be produced near the solidification front. External mechanical forces are applied by the pinch rolls, the bending rolls or the straightening rolls, mould oscillation, or misalignment of the mould and roller cages. In addition, the ferrostatic pressure inside the solidified shell applies a load. It can also cause bulging if the distance between the rolls is large (Grill et al., 1976).

Whatever their origins, the stresses can have a deleterious effect both on the casting operation and the quality of the cast product. If the stresses are sufficiently high and tensile in nature they can lead to the formation of a variety of surface and internal cracks. The types of cracks encountered in cast steel have been well documented in the literature by Grill et al. (1976). Of the two most general types, surface cracks are the most serious problem since they do not reweld and must be removed before rolling. Internal cracks are a lesser problem in this regard but must reweld fully to yield a completely sound rolled product.

The objective here is to discuss the application of the finite element method to investigate the stresses within the casting.

3-2 Finite Element Formulation

One of the most popular finite element formulations of elasticity starts by assuming a displacement field and then minimizes the potential energy to obtain the nodal values of the displacements. Once the displacements are known, it is possible to solve for the strains and stresses. Since the finite element formulation which was used in this analysis depends on the minimization of the potential energy, it is appropriate to give a complete statement of the theorem of potential energy (Segerlind, 1976):

> Of all displacements satisfying the given boundary conditions, those that satisfy the equations of equilibrium are distinguished by a stationary (extreme) value of the potential energy.

The important requirement of this theorem is that the displacement equations selected must satisfy the displacement boundary conditions and provide continuity in the displacements from one element to the next.

(

(

v

(.

wh

d.

en

The total potential energy of an elastic system can be separated into two components; a component resulting from the strain energy in the body and a component related to the potential energy of the internal and applied loads. The total potential energy, Π, can be written as

(3-1) $$\Pi = \Lambda + W_p$$

where Π is the strain energy and W_p is the potential of the applied loads. The work done by the loads is the negative of their potential energy or

(3-2) $$W = -W_p$$

Combining 3-1 and 3-2 yields:

(3-3) $$\Pi = \Lambda - W$$

Realizing that the region is subdivided into a number of elements, 3-3 is written in summation form

(3-4) $$\Pi = \sum_{e=1}^{n} (\Lambda^{(e)} - W^{(e)})$$

The strain energy for a differential element of volume dV is given by

(3-5) $$d\Lambda = \frac{1}{2}\{\varepsilon\}^T\{\sigma\} - \frac{1}{2}\{\varepsilon_0\}^T\{\sigma\}$$

where $\{\varepsilon\}$ is the total strain and $\{\varepsilon_0\}$ is an initial strain, $d\Lambda$ is called the strian energy density and the total strain energy is obtained by integration over the volume giving

$$\Lambda = \int_V \frac{1}{2}(\{\varepsilon\}^T\{\sigma\} - \{\varepsilon_o\}^T\{\sigma\})dv \tag{3-6}$$

The column vectors $\{\varepsilon\}$ and $\{\sigma\}$ in three-dimensional cases are:

$$\{\varepsilon\}^T = [\varepsilon_{xx} \quad \varepsilon_{yy} \quad \varepsilon_{zz} \quad \gamma_{xy} \quad \gamma_{yz} \quad \gamma_{xz}]$$

$$\{\sigma\}^T = [\sigma_{xx} \quad \sigma_{yy} \quad \sigma_{zz} \quad \tau_{xy} \quad \tau_{yz} \quad \tau_{xz}]$$

The basic course in the theory of elasticity (Timoshenko and Goodier, 1970) provides two important relationships; Hooke's law, which relates the stress and strain components, and the strain displacement relationship. Hooke's law has the general form

$$\{\sigma\} = [D]\{\varepsilon\} - [D]\{\varepsilon_o\} \tag{3-7}$$

where [D] contains the elastic material constants. The strain displacement relationshop in rectangular coordinates are

$$\begin{aligned}
\varepsilon_{xx} &= \frac{\partial U_x}{\partial x} & \gamma_{xy} &= \frac{\partial U_x}{\partial y} + \frac{\partial U_y}{\partial x} \\
\varepsilon_{yy} &= \frac{\partial U_y}{\partial y} & \gamma_{yz} &= \frac{\partial U_y}{\partial z} + \frac{\partial U_z}{\partial y} \\
\varepsilon_{zz} &= \frac{\partial U_z}{\partial z} & \gamma_{xz} &= \frac{\partial U_x}{\partial z} + \frac{\partial U_z}{\partial x}
\end{aligned} \tag{3-8}$$

and in cylindrical coordinates are

$$\text{(3-9)} \qquad \begin{aligned} \varepsilon_{rr} &= \frac{\partial U_r}{\partial r} & \gamma r\theta &= \frac{\partial U_r}{r\partial\theta} + \frac{\partial U_\theta}{\partial r} - \frac{U_\theta}{r} \\ \varepsilon_{\theta\theta} &= \frac{U_r}{r} + \frac{\partial U_\theta}{r\partial\theta} & \gamma rz &= \frac{\partial U_r}{\partial z} + \frac{\partial U_z}{\partial r} \\ \varepsilon_{zz} &= \frac{\partial U_z}{\partial z} & \gamma\theta z &= \frac{\partial U_z}{r\partial\theta} + \frac{\partial U_\theta}{\partial z} \end{aligned}$$

where U_x, U_y, U_z and the displacement components in the x, y and z coordinate directions, and U_r, U_Θ and U_z are the displacement components in r, θ and z (cylindrical) coordinate directions. These displacement components can be writttern in terms of the nodal values using the same three-dimensional prism as used in Chapter Two,

(3-10)

$$\begin{Bmatrix} U_x \\ U_y \\ U_z \end{Bmatrix} = \begin{bmatrix} N_1 & 0 & 0 & N_2 & 0 & 0 & \cdots\cdots & N_{20} & 0 & 0 \\ 0 & N_1 & 0 & 0 & N_2 & 0 & \cdots\cdots & 0 & N_2 & 0 \\ 0 & 0 & N_1 & 0 & 0 & N_2 & \cdots\cdots & 0 & 0 & N_{20} \end{bmatrix} \begin{Bmatrix} U_1 \\ U_2 \\ U_3 \\ U_4 \\ U_5 \\ \cdot \\ \cdot \\ \cdot \\ \cdot \\ U_{58} \\ U_{59} \\ U_{60} \end{Bmatrix}$$

where U_1, U_2 and U_3 are the displacement components in x, y and z direction (or r, θ and z direction in cylindrical coordinates) for node one. U_4, U_5 and U_6 are the displacement components in x, y and z directions (or r, θ and z direction in cylindrical coordinates) for node two, and likewise up to U_{58}, $_{59}$ and U_{60} for node twenty. The general form of the equation 3-10 is

$$\{U\} = [N]\{U\} \tag{3-11}$$

where [N] is a 3 x 60 matrix containing the shape functions. The application of 3-8 (3-9) allows the strain vector $\{\varepsilon\}$ be written in terms of the nodal displacements {U}. The general form of this relationship is

$$\{\varepsilon\} = [B]\{U\} \tag{3-12}$$

where [B] is derived by performing the proper differentiation of [N]. In rectangular coordinates [B] is

$$[B] = \begin{bmatrix} \partial N_i/\partial x & 0 & 0 \\ 0 & \partial N_i/\partial y & 0 \\ 0 & 0 & \partial N_i/\partial z \\ \partial N_i/\partial y & \partial N_i/\partial x & 0 \\ 0 & \partial N_i/\partial z & \partial N_i/\partial y \\ \partial N_i/\partial x & 0 & \partial N_i/\partial z \end{bmatrix} \quad i=1,20 \tag{3-13}$$

and in cylindrical coordinates is

$$[B] = \begin{bmatrix} \partial N_i/\partial r & 0 & 0 \\ N_i/r & \partial N_i/r\partial\theta & 0 \\ 0 & 0 & \partial N_i/\partial z \\ \partial N_i/r\partial\theta & \partial N_i/\partial r - N_i/r & 0 \\ \partial N_i/\partial z & 0 & \partial N_i/\partial r \\ 0 & \partial N_i/\partial z & \partial N_i/r\partial\theta \end{bmatrix} \quad i=1,20 \tag{3-14}$$

The materials property [D] for a three-dimensional isotropic material is

$$[D] = \frac{E(1-\mu)}{(1+\mu)(1-2\mu)} \times \tag{3-15}$$

$$\begin{bmatrix} 1 & \mu/(1-\mu) & \mu/(1-\mu) & 0 & 0 & 0 \\ & 1 & \mu/(1-\mu) & 0 & 0 & 0 \\ & & 1 & 0 & 0 & 0 \\ & & & \frac{1-2\mu}{2(1-\mu)} & 0 & 0 \\ & \text{SYM} & & & \frac{1-2\mu}{2(1-\mu)} & 0 \\ & & & & & \frac{1-2\mu}{2(1-\mu)} \end{bmatrix}$$

where E is the elastic modulus and μ is Poisson's ratio.

Utilizing equations 3-7 and 3-12, the strain energy $\Lambda^{(e)}$ for a single element can be written as

$$\Lambda^{(e)} = \int_{V^{(e)}} \frac{1}{2}(\{U\}^T[B^{(e)}]^T[D^{(e)}][B^{(e)}]\{U\} - 2\{U\}^T[B^{(e)}]^T[D^{(e)}]\{\varepsilon_o^{(e)}\} + \{\varepsilon_o^{(e)}\}^T[D^{(e)}]\{\varepsilon_o^{(e)}\})dv \tag{3-16}$$

The work done by the applied loads can be separated into three distinct parts: that which is due to the concentrated loads, W_c; that which results from the stress components acting on the outside surface, W_p; and that which is done by the body forces, W_b (Segerlind, 1976).

$$W_c = \{U\}^T\{P\} = \{P\}^T\{U\} \tag{3-17}$$

$$\overset{(e)}{W_b} = \int_{\overset{(e)}{v}} \{U\}^T[\overset{(e)}{N}]^T \begin{Bmatrix} X_b \\ Y_b \\ Z_b \end{Bmatrix} dv \tag{3-18}$$

$$\overset{(e)}{W_p} = \int_{\overset{(e)}{s}} \{U\}^T[\overset{(e)}{N}]^T \begin{Bmatrix} P_x \\ P_y \\ P_z \end{Bmatrix} ds \tag{3-19}$$

where $\{P\}$ is the concentrated force which has been resolved into components parallel to the displacement components. X_b, Y_b and Z_b are the components of body forces and P_x, P_y and P_z are the stress components parallel to the x, y and z coordinate directions.

The combination of equations 3-4, 3-16, 3-17, 3-18 and 3-19 yields the total potential energy Π. To minimize the Π, one can differentiate Π with respect to $\{U\}$ and set that equal to zero. So

$$\begin{aligned} \frac{\partial \Pi}{\partial \{U\}} = \sum_{e=1}^{n} \Bigg[& \int_{\overset{(e)}{v}} [\overset{(e)}{B}]^T[\overset{(e)}{D}][\overset{(e)}{B}]dv\{U\} \\ & - \int_{\overset{(e)}{v}} [\overset{(e)}{B}]^T[\overset{(e)}{D}]\{\varepsilon_o\}dv - \int_{\overset{(e)}{v}} [\overset{(e)}{N}]^T \begin{Bmatrix} X_b \\ Y_b \\ Z_b \end{Bmatrix} dv \\ & - \int_{\overset{(e)}{s}} [\overset{(e)}{N}]^T \begin{Bmatrix} P_x \\ P_y \\ P_z \end{Bmatrix} ds \Bigg] - \{P\} = 0 \end{aligned} \tag{3-20}$$

The components of the concentrated forces are not included within the summation because the forces are located at the nodes.

The integrals in 3-20 define the element matrices that consist of an element stiffness matrix [ESM] and an element force vector {EF}, which combine in the form

(3-20a) $$\frac{\partial \Pi^{(e)}}{\partial \{U\}} = [ESM^{(e)}]\{U\} + \{EF^{(e)}\} = 0$$

where (3-21) $$[ESM^{(e)}] = \int_{v^{(e)}} [B^{(e)}]^T [D^{(e)}][B^{(e)}] dv$$

and (3-22) $$\{EF^{(e)}\} = - \int_{v^{(e)}} [B^{(e)}]^T [D^{(e)}]\{\Delta T^{(e)}\} dv - \int_{v^{(e)}} [N^{(e)}] \begin{Bmatrix} X_b \\ Y_b \\ Z_b \end{Bmatrix} dv - \int_{s^{(e)}} [N^{(e)}]^T \begin{Bmatrix} P_x \\ p_y \\ P_z \end{Bmatrix} ds - \{P\}$$

To use the numerical integration technique, a transformation must be made from rectangular coordinates to natural coordinates (as discussed in Chapter Two). Equations 3-21 and 3-22 become

(3-23) $$[ESM^{(e)}] = \sum_{i=1}^{3} \sum_{J=1}^{3} \sum_{k=1}^{3} \left[f_1(\xi_i, \eta_J, \zeta_k) H_{iJk} |\det[J]| \right]$$

and

$$\{EF\}^{(e)} = -\sum_{i=1}^{3}\sum_{J=1}^{3}\sum_{k=1}^{3}\left\{\left[f_2(\xi_i,\eta_J,\zeta_k)H_{iJk}+f_3(\xi_i,\eta_J,\zeta_k)H_{iJk}\right]\left|\det[J]\right|\right\}$$

(3-24)

$$-\sum_{i=1}^{3}\sum_{J=1}^{3}\left[f_4(\xi_i,\eta_J)H_{iJ}\left|\det[J_s]\right|\right]$$

where

$$f_1(\xi_i,\eta_J,\zeta_k) = [B]^T[D][B]$$

$$f_2(\xi_i,\eta_J,\zeta k) = [B]^T[D]\{\Delta T\}$$

$$f_3(\xi_i,\eta_J,\zeta_k) = [N]^T \begin{Bmatrix} X_b \\ Y_b \\ Z_b \end{Bmatrix}$$

and $f_4(\xi_i,\eta_J) = [N]^T \begin{Bmatrix} P_x \\ P_y \\ P_z \end{Bmatrix}$

The transformation must also be made for the integrals in cylindrical coordinates. From calculus, the determinant of the new Jacobian is

(3-25) $$\left|\det[J]\right| = r$$

The numerical integration for the integrals in the cylindrical coordinate is

(3-26) $$[ESM]^{(e)} = \sum_{i=1}^{3}\sum_{J=1}^{3}\sum_{k=1}^{3}\left[f_1(\xi_i,\eta_J,\zeta_k)H_{iJk}\left|\det[J]\right|r\right]$$

and

$$\{EF\}^{(e)} = -\sum_{i=1}^{3}\sum_{J=1}^{3}\sum_{k=1}^{3}\left\{\left[f_2(\xi_i,\eta_J,\zeta_k)H_{iJk} - f_3(\xi_i,\eta_J,\zeta_k)H_{iJk}\right]|\det[J]|r\right\}$$

(3-27)

$$-\sum_{i=1}^{3}\sum_{J=1}^{3}\left[f_4(\xi_i,\eta_J)H_{iJ}|\det[J]|r\right]$$

where r is the radius of the curvature to integration point and is defined at any point by

(3-28)

$$r = \sum_{i-1}^{20} N_i r_i$$

where r_i is the distance of each node to the center of the curvature.

3.3 Boundary Conditions

3.3.1 Internal Forces. Ferrostatic pressure, which produces stresses in the solidifying skin must be examined together with the shrinkage of the casting. As the casting shrinks from the mould, the ferrostatic pressure tends to bulge the casting until contact with the mould is restored. As a result of the bulging, both bending and membrane stresses are developed in the casting (Lankford, 1972). Once the casting exists in the mould, there is no longer a continuous restraint to bulging, and if the guide rolls and the drive rolls are too widely spaced, bulging might occur to the extent that the casting tears, ruptures, or deforms and becomes too large to pass through the rolls.

The weight of the casting or the gravity force of the solidified casting contributes axial stress to the skin. Without an outside influence from the drive rolls, the unsupported weight of the cast below any specified level of the cast would be resisted completely by axial tension in the cast above that level. The value of density of steel was assumed to be constant and 7.4 gr/cm^2.

3.3.2 External Forces. Mould friction forces: Most continuous casting moulds are oscillated to prevent "welding" or "sticking" of the cast metal to the mould, which produces a high apparent friction and tearing of the solidifying skin. However, some friction occurs in oscillating moulds and this leads to stresses in the skin. When the velocity of the casting relative to the mould wall is downward, an upward friction force acts on the skin surface, as illustrated in Figure 3-1. This friction force depends on the coefficient of friction and the ferrostatic force. The coefficient of friction depends on mould roughness, mould material, and lubrication. Due to lack of information in the magnitude of the coefficient of friction, the friction force within the mould was neglected in this study.

Guiding roll friction forces are not important in the straight portion due to clearance between rolls and casting. These rolls are important in the curved portion because most of the weight of the casting has to be carried by these rolls. The roller friction forces depend on the space between rolls, the coefficient of the friction of the roll bearings and whether the casting has any tearing or not. The friction force resulting from the rollers was also ignored because of a lack of information on its value.

Drive rolls exert a tractive force that can counteract or add to the gravity force. If the tractive effort of the drive rolls tends to draw the casting then the effective axial tensile force at a specific point is the weight of the casting below this point plus the tractive effort. If the tractive effort of the drive rolls tends to compress or upset the casting, then the effective axial force is the weight minus the tractive effort and may range from a tension level less than the gravity force to compression.

Bending rolls and straightening rolls at the beginning and the end of the curved portion will force the casting to be displaced in the direction of the radius of the curvature. Figure 3-2 shows the location of these two forces. The magnitude of these displacements depends on the radius of the curvature.

Other sources of stress can arise from mechanical inaccuracies or operational irregularities.

3.3.3 Known Displacements. In the straight portion, the displacements on the face indicated by A on Figure 3-3a in the x direction and the displacements on the face denoted by B in the y direction are zeroes because of

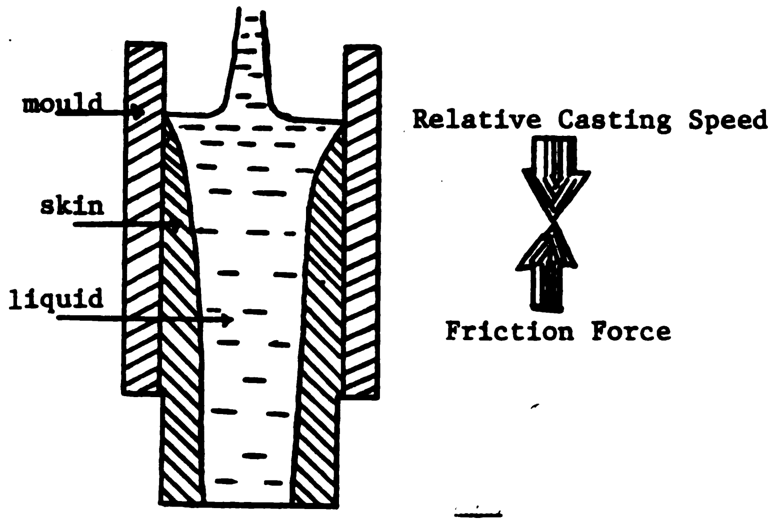

Figure 3-1 Direction of friction force at mould.

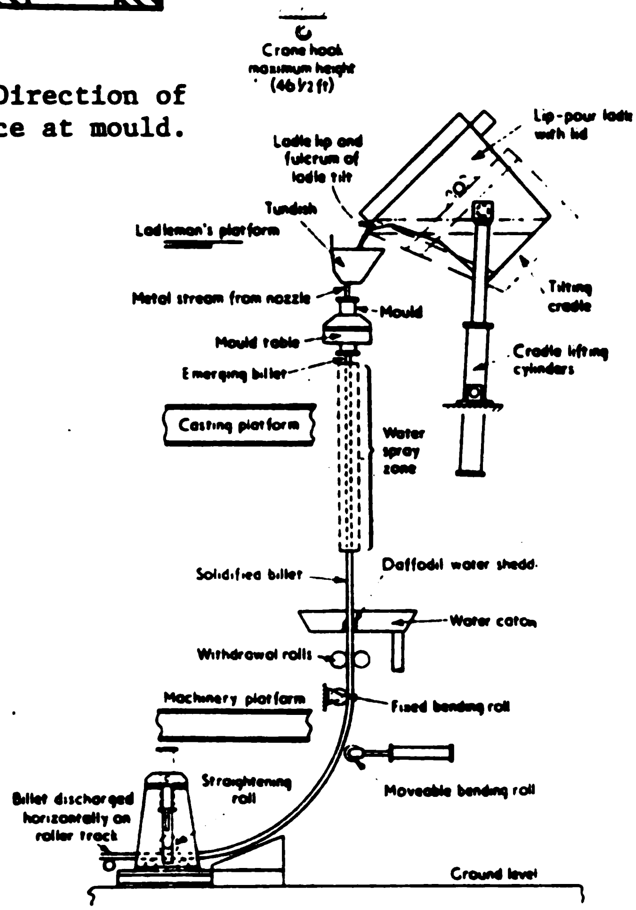

Figure 3-2 An approximation of location of the various rolls.

symmetry. The displacements on the face indicated by C on Figure 3-3b in the direction of Z were assumed to be zero. The contact point between the guidance rolls and casting make a set of zero displacements in the direction of the radius of the curvature.

3.4 Material Properties

In order to calculate the stresses in the solidifying shell of a continuously cast steel section, the following mechanical properties must be known between about 800^{o}C and the solidifying temperature: a) Young's modulus, E; b) the strain limit of elasticity, ε_{el} (or yield stress σy); c) Poisson's ratio, υ.

Although numerous measurements of these properties have been made for steel at lower temperatures, very few measurements have been undertaken over the temerature range of interest to continuous casting. One reason for this lack of activity is the fact that steels are not used at high temperatures, another is simply the difficulty of performing experiments at these temperatures. Owing to the lack of experimental data, the magnitude and dependence on temperature of the mechanical properties had to be assumed, using existing data as a guide wherever possible. The values adopted for E, ε_{el} and υ were assumed as follows:

I. Young's modulus. E was assumed to vary linearly within temperatures according to a relationship given by Koster (1948).

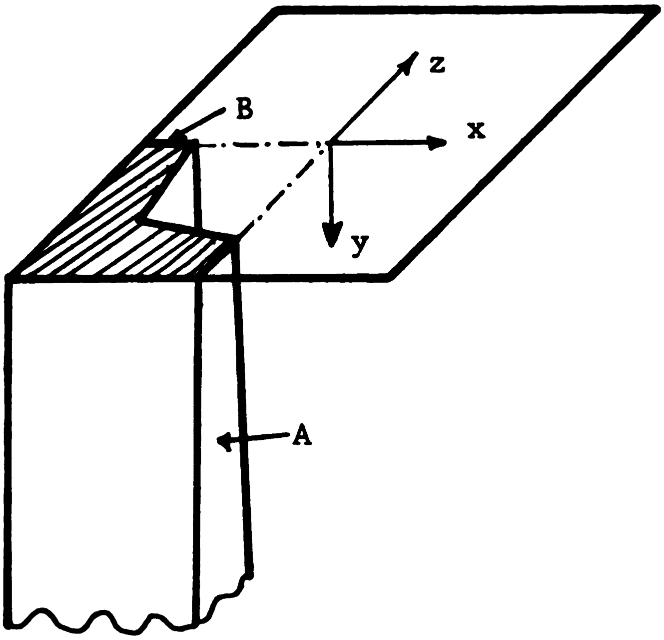

Figure 3-3(a) Location of cartesion coordinate at straight part of casting.

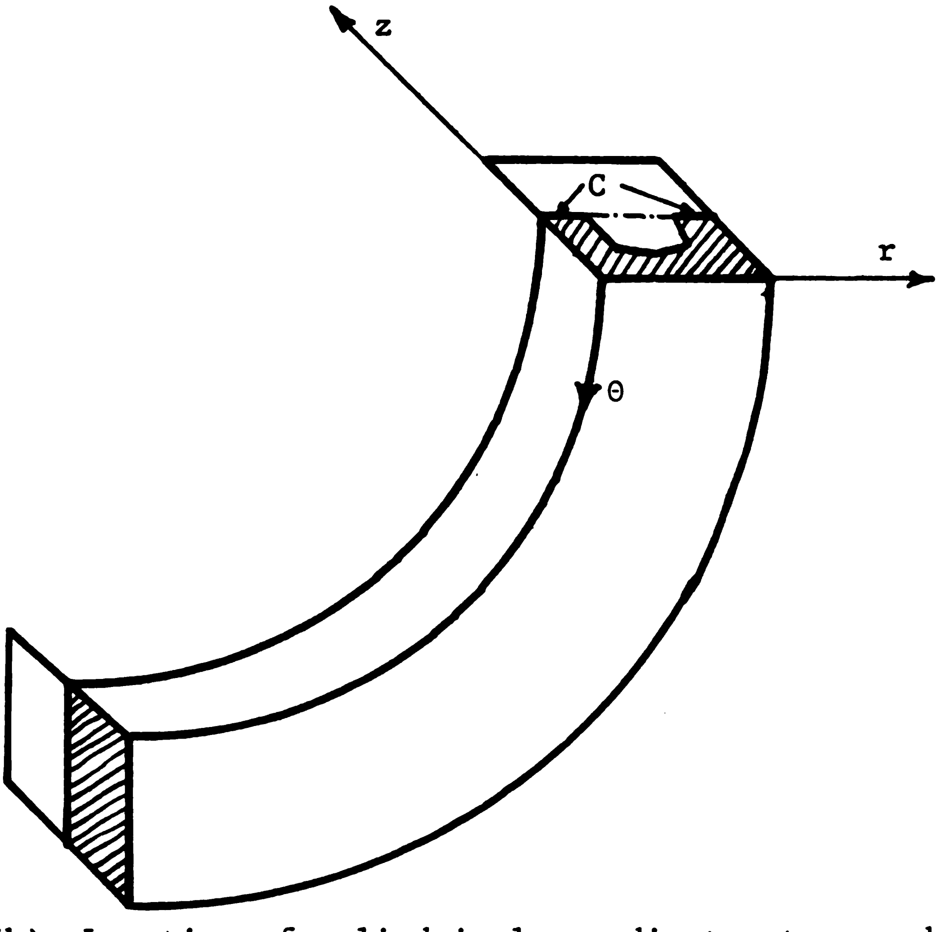

Figure 3-3(b) Location of cylindrical coordinate at curved part of casting.

$$E = 1.08x10^{6} - 0.103(T-T_{Tr})x10^{4} \quad Kg/cm^{2}$$

for temperatures in excess of $800^{\circ}C$ where T_{Tr} is the A3 transformation temperature, which varies with carbon content of the steel. In using values of E for pure iron in the mathematical model, it must be assumed that iron and steel have a similar elastic behavior. There is some evidence in support of this, since measured values of E for steel at lower temperatures are similar to those for iron, the dependence on temperature is also the same (Koster, 1948).

II. Strain limit of elasticity. ε_{el} was assumed to be 0.1% at $800^{\circ}C$ decreasing to roughly 0.05% at the solidified temperature T_s (Grill et al., 1977). In mathematical form the assumed temperature dependence of ε_{el} is written as:

$$\varepsilon_{el} = 1.47x10^{4} - 8.00Tx10^{8} \quad For\ T>1100^{\circ}C$$

$$\varepsilon_{el} = 4.84x10^{4} - 3.68Tx10^{7} \quad For\ T<1100^{\circ}C$$

III. Poisson's ratio. Since υ is knwon to be insensitive to variations in temperature for steel under elastic conditions, its value had been assumed to be constant ($\upsilon = 0.33$)(Grill et al., 1977).

Owing to the uncertainty resulting from these assumed mechanical properties, it is difficult to calculate values of stress that are absolutely correct. Nevertheless, it seems certain that the relative magnitude of the ratio of the calculated stress to yield stress can be used to interpret the complex deformation that is due to mechanical or thermal stresses and can cause internal or surface cracking of the steel.

IV. COMPUTER PROGRAMMING AND NUMERICAL RESULTS OF THE HEAT TRANSFER ANALYSIS

4-1 Computer Programming

In order to solve the equations presented in Chapter Two, a computer program with the following steps was generated: 1) read the number of elements, the number of equations, the band width, and generate the element data, 2) input an initial temperature distribution for the casting, 3) calculate the element stiffness matrix and the element force vector for each element and assemble these into a system of equations, 4) modify the system of equations to incorporate specified temperatures, and then solve the equations for the nodal temperature values, and 5) compare the nodal temperatures with the assumed temperatures at step two. If the maximum difference between the temperatures at any one node is less than $5^{\circ}K$, write the nodal temperatures and end the program. Otherwise, replace the old temperature values by the calculated values and then repeat step three through five, until the maximum difference drop between any successive pair of temperatures is less than $5^{\circ}K$.

A more detailed discussion of these steps is presented here.

4.1.1 Geometry. The existence of the symmetry allowed the analysis to be done using only one-eighth of the total cross-section. Figure 4-1 shows an analyzed cross-section and related dimensions. The division into elements is shown in Figure 4-2. The computer central memory storage would allow only twelve layers of elements (as shown in Figure 4-2) along the direction of casting. Therefor, to simulate the whole casting the height of the element (in the z direction) was much larger than the x and y dimensions (in cross-section). The twelve layers along the casting direction had seventy two elements with the five hundred fifty nine nodes and the band width of the system of equations was fifty eight. There was one equation for each node. The height of the elements (dimension in the z direction) was 50 cm.

4.1.2 Initial Temperatures. The material properties and effective radiation heat transfer coefficient are dependent on the casting temperature. At any point within or on the surface of an element the temperature was calculated using

$$T_p = \sum_{i=1}^{20} T_i N_i$$

where the N_i are the element shape functions, and T_i are the element nodal temperatures. A first solution was obtained by assuming a temperature distribution for the casting. This could be any reasonable guess. After the first solution, the assumed values were replaced by the

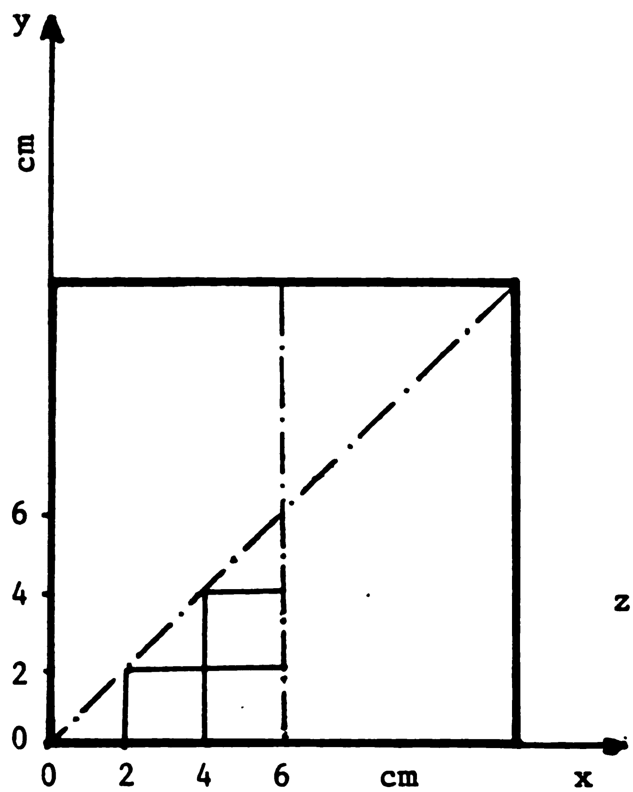

Figure 4-1 Dimension of the Elements in x-y cross-section.

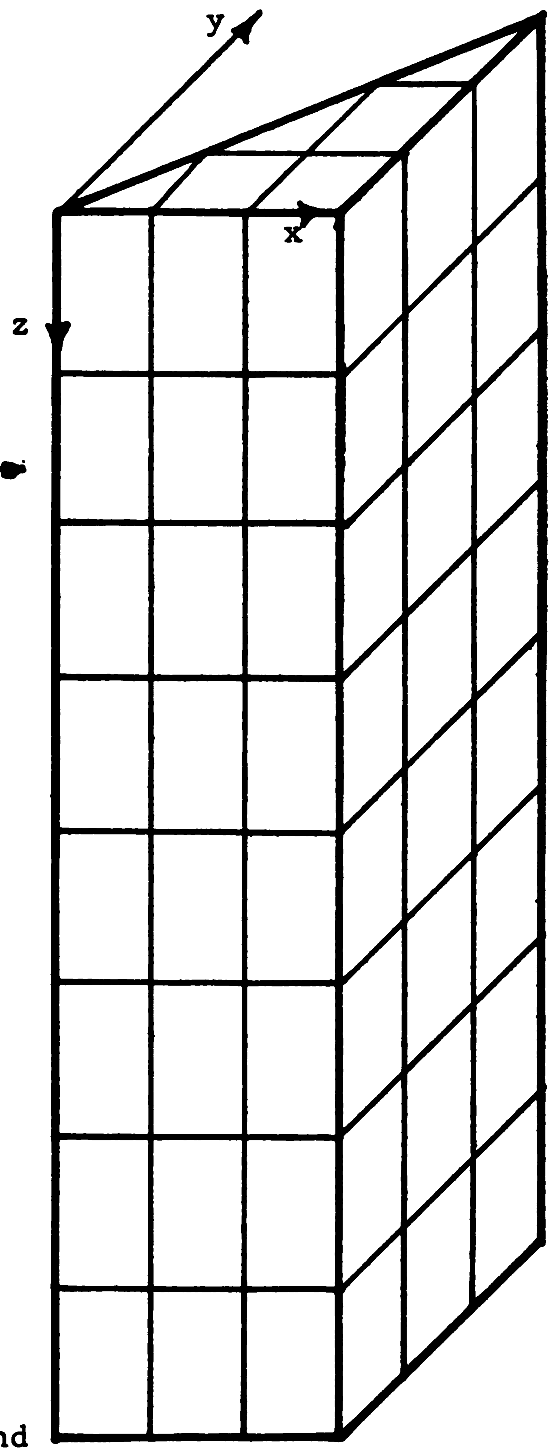

Figure 4-2 Division into the elements and location of the coordinates. (Dimension in x and y are expanded)

newly calculated temperatures, and the analysis continued until the correct temperatures within ± 5°K were obtained.

4.1.3 Element Stiffness Matrix and Element Force Vector. A subroutine was written to evaluate the element matrices using equations 2-12 and 2-13 and the boundary conditions 2-3, 2-4 and 2-5. The subroutine had several options to handle heat loss from a specific side by spray cooling or radiation.

4.1.4 Solution. The element matrices were assembled into a banded system of equations. The zero coefficients outside the band width were not stored. The banded system of equations were unsymmetrical. It was observed, however, that the diagonal terms in the system of equations were such that the round off error was not large if the equations were solved without pivoting. The pivoting of elements was not done during the solution because pivoting requires full storage of the system of equations to obtain a solution. The requirement of full storage of the system of equations would have used a lot of additional computer memory space.

When the assembly of the system of equations was completed, the equations were modified for the known boundary temperatures. A Gausian elimination method was used to solve the system of equations.

A set of assembly, modification and solution subprograms was developed to handle the unsummetrical stiffness matrix.

4.2 Input to the Program

4.2.1 General. A 12x12 cm cross-section casting was analyzed, and the division into elements was as shown in Figure 4-2. This size of cross-section was one of the most popular commercial billets which are continuously cast. The other information such as thermophysical properties and casting velocity were also representative of values which are used in industry.

The solidus temperature for a typical commercial steel was 1770°K and the liquidus temperature was 1800°K (Lait et al., 1974). The incoming molten metal after being poured into the mould was also assumed to be 1800°K. The casting velocity was specified at 3 cm/sec, and kept constant.

4.2.2 Boundary Conditions. The temperature of the nodes at the upper face of the first layer was assumed to be 1800 K. The heat transfer by the mould cooling water was defined as

$$q = (640 - 80\sqrt{t})(.418) \text{ Joules cm}^{-2}\text{s}^{-1} \tag{4-1}$$

(Brimacombe et al., 1974) where t was the average time each element in contact with the mould was in the mould. The value of t for each contacting element was calculated using the distance of the middle of that element from the top of the mould divided by the casting velocity (Lait et al., 1974).

The mould was assumed to be 50 cm deep, perfectly square in cross-section, and straight in the direction of the casting. All types of heat transfer within the mould are incorporated in equation 4-1.

The secondary cooling zone using a water spray was applied right after the mould and was assumed to be a multihank spray cooler. A ¼ GG 10 nozzle with a water spray pressure (1.26 N/cm^2) and water flux 1172 $LIT/sec\text{-}cm^2$ was used in the first 1.5 meters after the mould. The heat transfer coefficient for these conditions of nozzle and water flux was reported by Mizikar (1970) to be 0.17 w/cm -°K. This stage was followed by another 1.5 meters of spray using a lower spray pressure with the heat transfer coefficient of 0.14 w/cm -°K. The third stage consisted of one meter with a heat transfer coefficient of 0.11 w/cm -°K.

The radiation cooling zone had a heat transfer coefficient defined by

$$h_{rad} = \sigma_s \varepsilon_e (T_s - T_{inf})(T_s^2 + T_{inf}^{\ 2}) \tag{4-2}$$

The T_{inf} or overall surrounding temperature to which heat was assumed to be 675°K because of the hot working conditions around the casting.

The results of this program are presented in Figure 4-3. The solid line shows the temperature distribution at one corner of the cross-section, the dotted line shows the

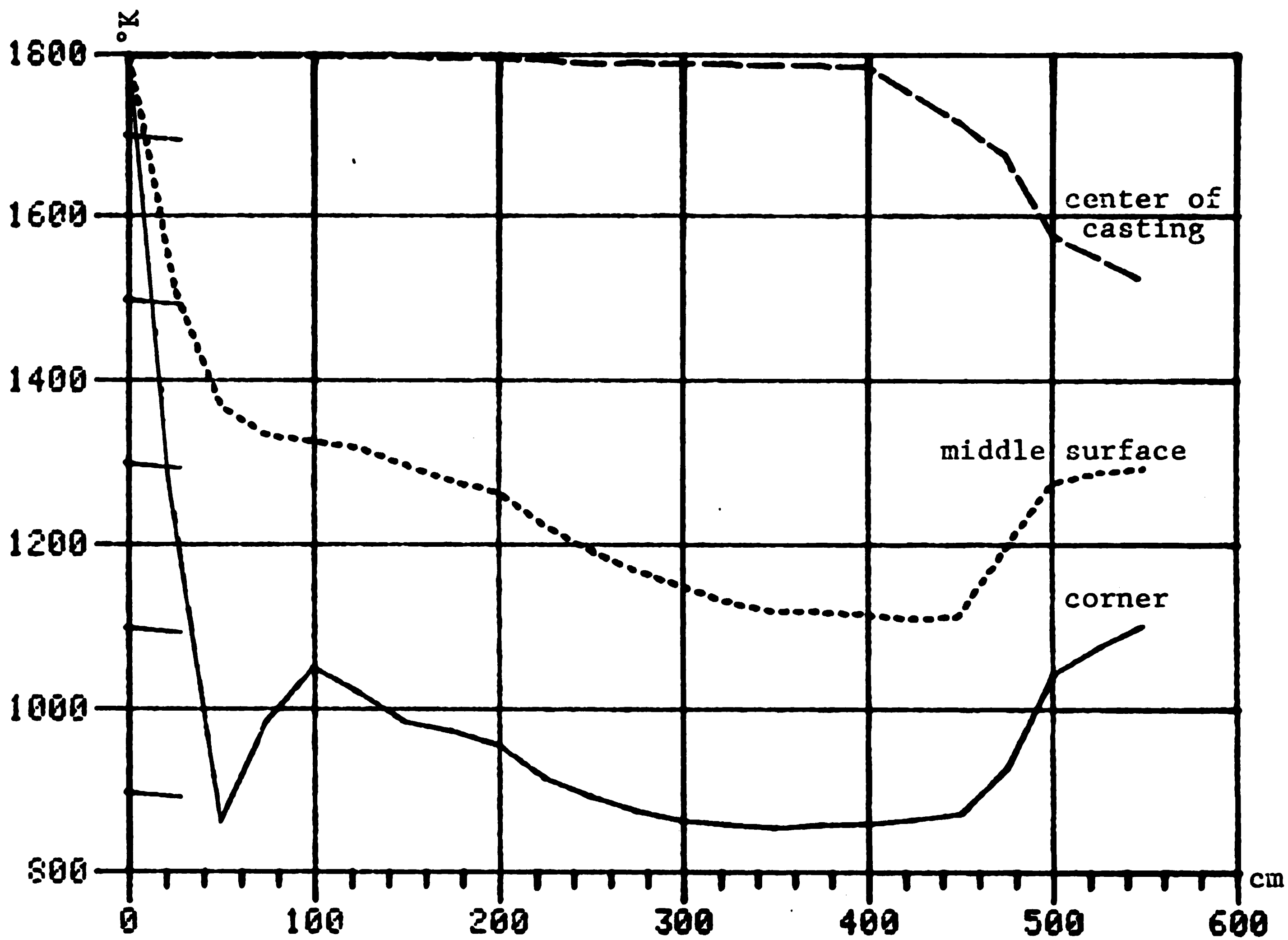

Figure 4-3 Temperature distribution along z direction of casting.

temperature distribution at the side surface, and the dashed line is for the center of the casting.

The fifty centimeter height of the elements gave temperature information every twenty five centimeters along the z direction (the direction of the casting). To get the temperature distribution in the z direction every few centimeters required the casting be divided into twelve segments. The division into segments is justified on the basis that the heat flux in the z direction is much lower than it is in the x and y directions (Raychaudhuri, 1974, and Lait et al., 1974). Figure 4-3 shows that after the mould and before complete solidification the temperature decreases about 0.5°K for each centimeter in the direction of the casting. The difference between temperatures at the center of the casting and the surface (dashed line and dotted line, respectively) at any point after the mould and before complete solidification is about 100°K for each centimeter in either the x or y directions.

The twelve segments of the casting were analyzed each in a separate piece. For any piece the same program simulated 75 cm of the casting along the z direction but only the upper 50 cm were accepted. Each segment was divided into the twelve layers of elements and the height of the element was the only change in the main program (6.125 cm). Dividing the casting into segments required an insulated boundary at the bottom of each part, and also assumed the heat flow in the z direction was not important compared to heat flow in the x and y directions. The temperature distribution of the top of the first portion was assumed to be 1800 K (incoming liquid materials). The temperature distribution at the top of the next portion was assigned to the temperature of the cross-section located 50 cm deep in the previous portion. The remaining 25 cm of each segment were overlapped by the new one. The assumption of an insulated boundary at the bottom of the segments could raise the temperatures near by the insulated area. The overlap was done to reduce this error (Figure 4-4).

The simulation of the casting as a series of steps was necessary because of the limitation of the computer central memory and the need to get temperature data at closer intervals for the elasticity study. The results of the segments after overlapping are shown in Figure 4-5. Figure 4-6 compares the results of the whole casting at one step and the stepwise solutions. The agreement is good. A check also has been done by comparing the results of the overlapped piece in the casting in two steps. The overlapped nodes in step four are shown in Figure 4-7. The difference of $\pm 1^{o}$K in Figure 4-7 shows the overlapped nodes.

4.3 Results and Comparison

The temperature distribution along the z direction obtained from the large elements and the stepwise solution is shown in Figure 4-3 and 4-5. Figure 4-8 shows the shell

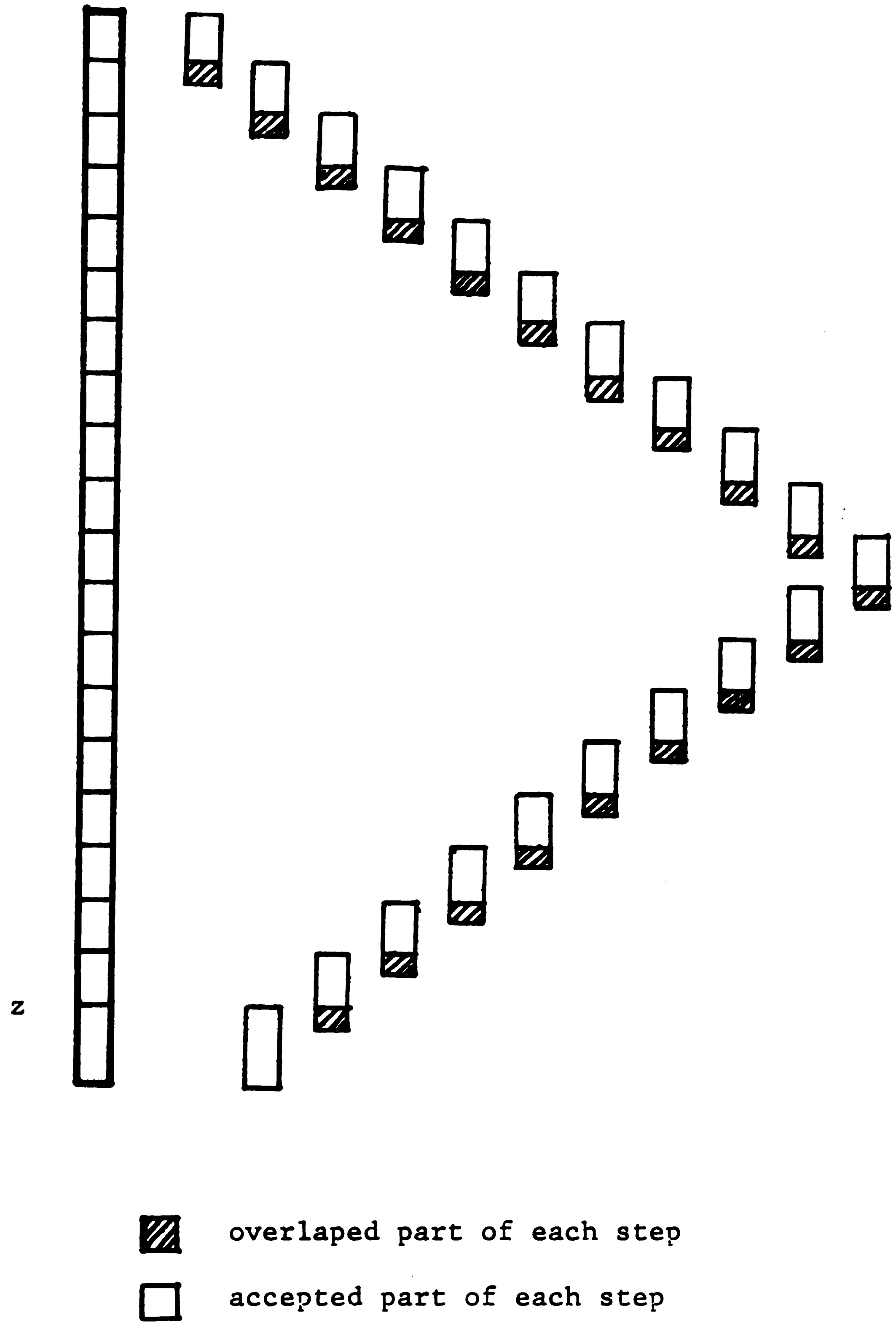

Figure 4-4 Portion along the z direction with overlap.

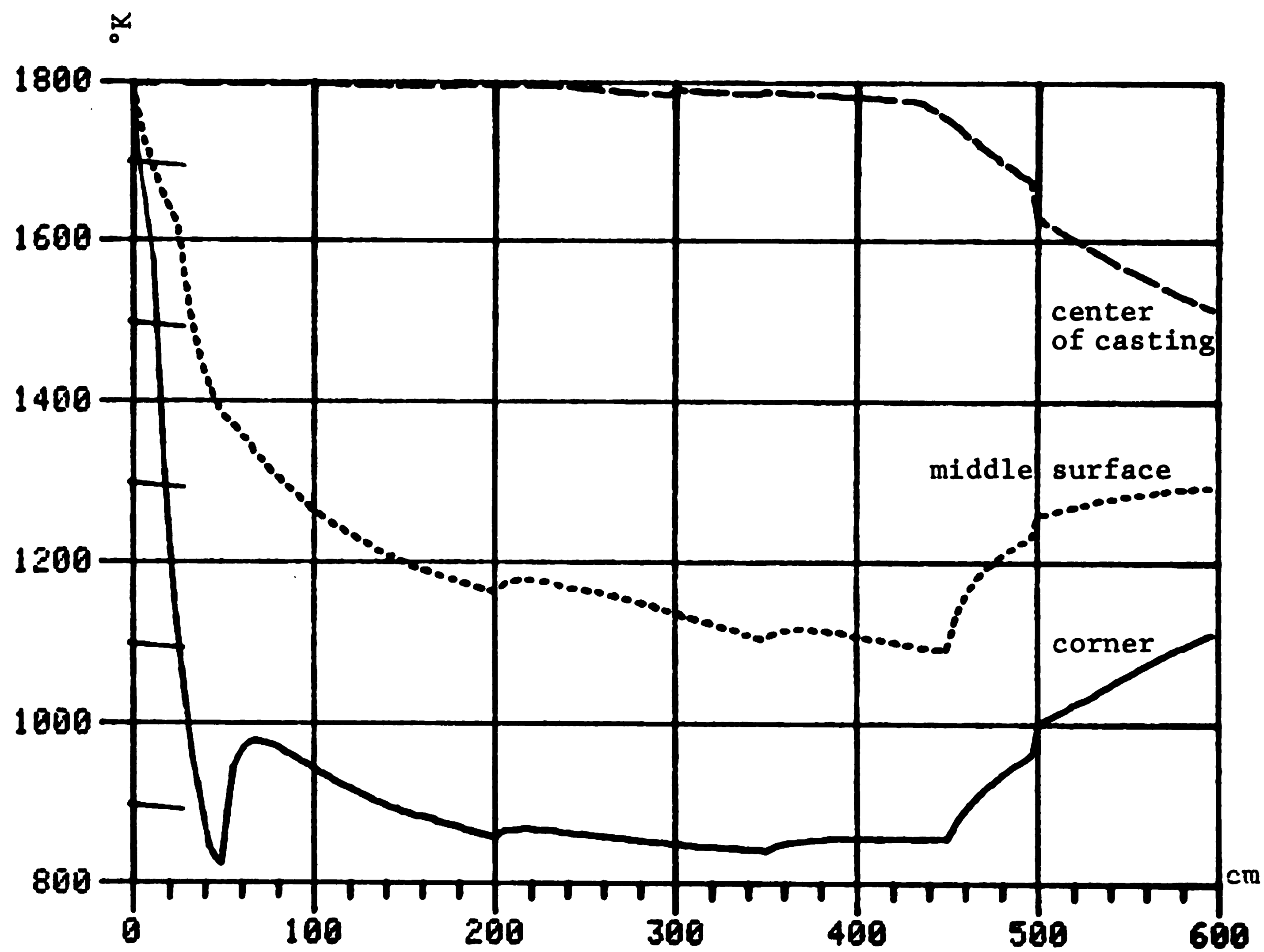

Figure 4-5 Temperature distribution along z direction of casting

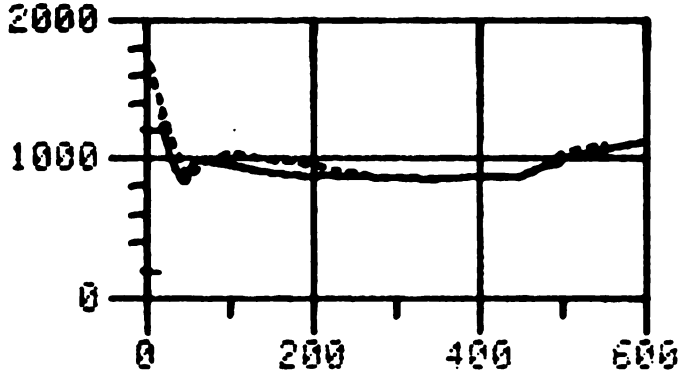

A - corner temperature

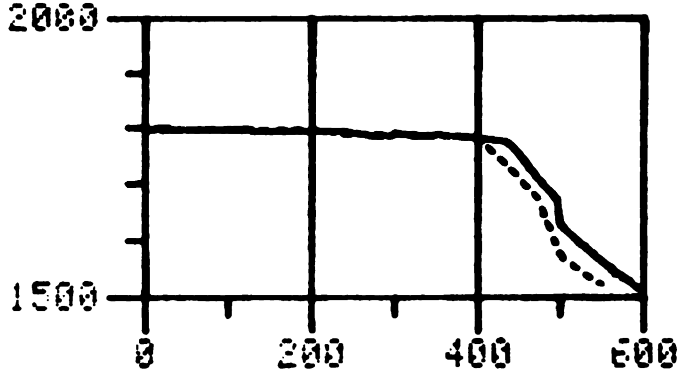

C - center temperature

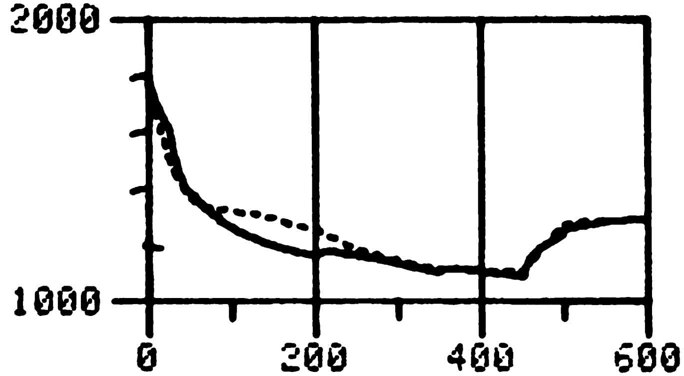

B - middle surface temperature

Stepwise solution in solid line and one solution in dotted line.

Figure 4-6 Difference of the temperature between one solution and step wise solution along z direction.

1229	1720	1796	1797					
1221	1714	1796	1797					
1214	1709	1796	1797					
1207	1703	1796	1796					
1200	1698	1796	1796		1200	1698	1796	1796
1195	1692	1796	1796		1195	1693	1796	1796
1191	1686	1795	1796		1191	1686	1795	1796
1186	1680	1794	1796		1186	1680	1794	1796
1182	1675	1794	1796		1181	1675	1793	1796
					1177	1669	1793	1796
					1172	1664	1792	1797
					1168	1660	1792	1797
					1164	1655	1791	1797

Step #3 Step #4

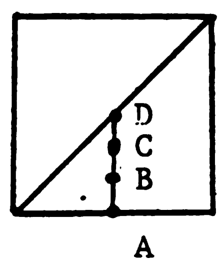

Figure 4-7 Comparison of the overlaped nodes between step three and step four. Loaction of the selected points for comparison.

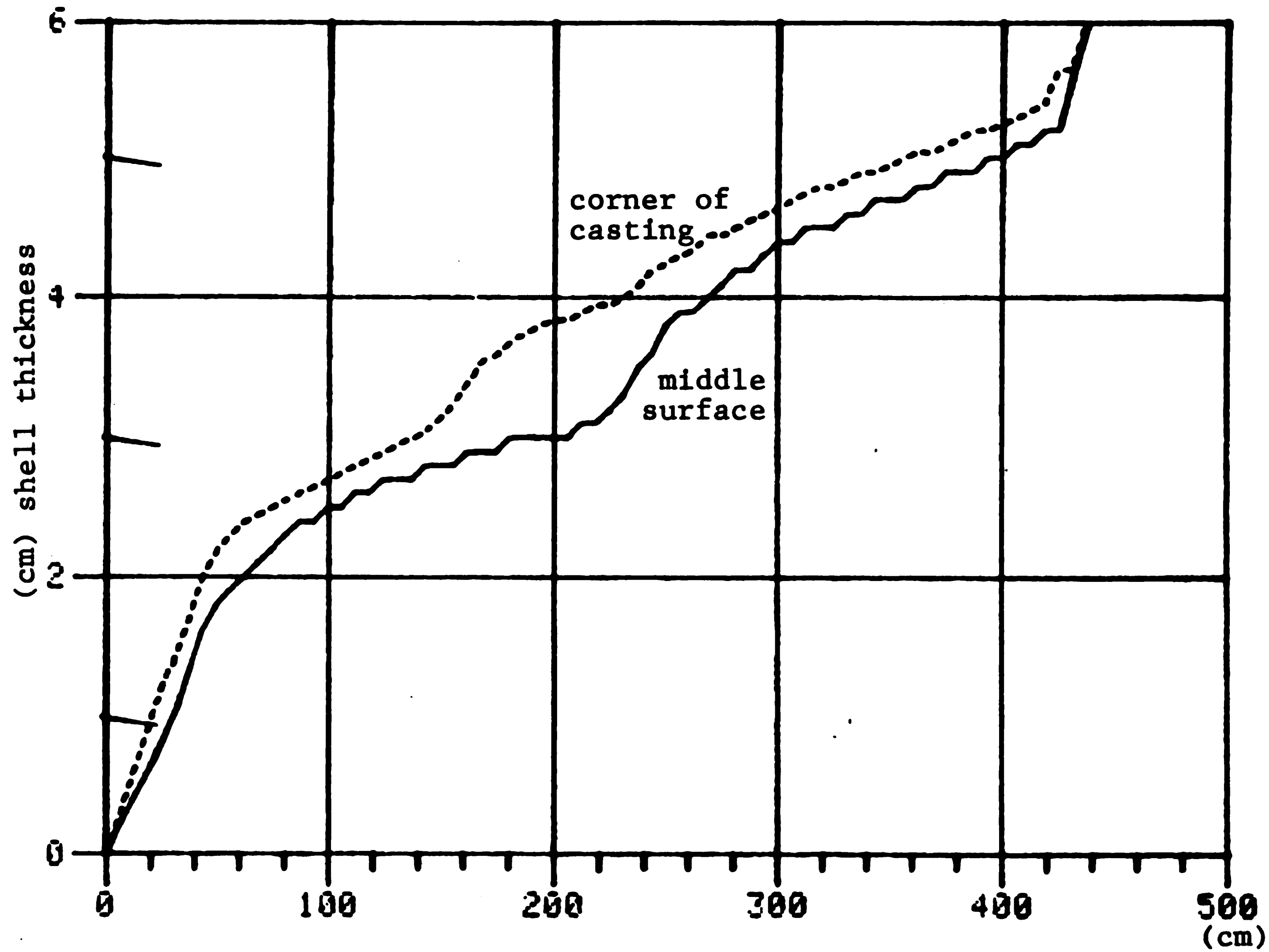

Figure 4-8 Shell thickness along z direction.

thickness in centimeters along the casting direction. From Figure 4-3 the corner points are experiencing the maximum thermal variations, but the center of the casting has almost no temperature change until the last drop of liquid solidifies. Figures 4-9 and 4-10 show the temperature contour lines in the cross-section at the exit of the mould and at the place of complete solidification, respectively. Figure 4-11 shows the contour lines in the x-z directions at the bottom of the spray cooling water zone. Once the complete solidification occurs, the center temperature decreases rapidly. The length of the ingot required for complete solidification under the conditions listed in this chapter was calculated to be 440 cm. The shell thickness just outside the mould was 1.8 cm.

Mathew (1976) reported the temperature of the casting surface at the exit mould at 1483°K for his axisymmetric model. Lait et al. (1974) reported the calculated temperature at the exit of the mould, using a two-dimensional finite difference method, at 1407°K. The measured temperature of the ingot surface at the exit of the mould was 1330°K (Lait et al., 1974) and 1375°K (Gautier et al., 1970). The temperature calculated at the mould exit in this study was 1350°K for the middle of the surface of the ingot. This is the only calculated value that can be compared with other reported results because of differences in boundary

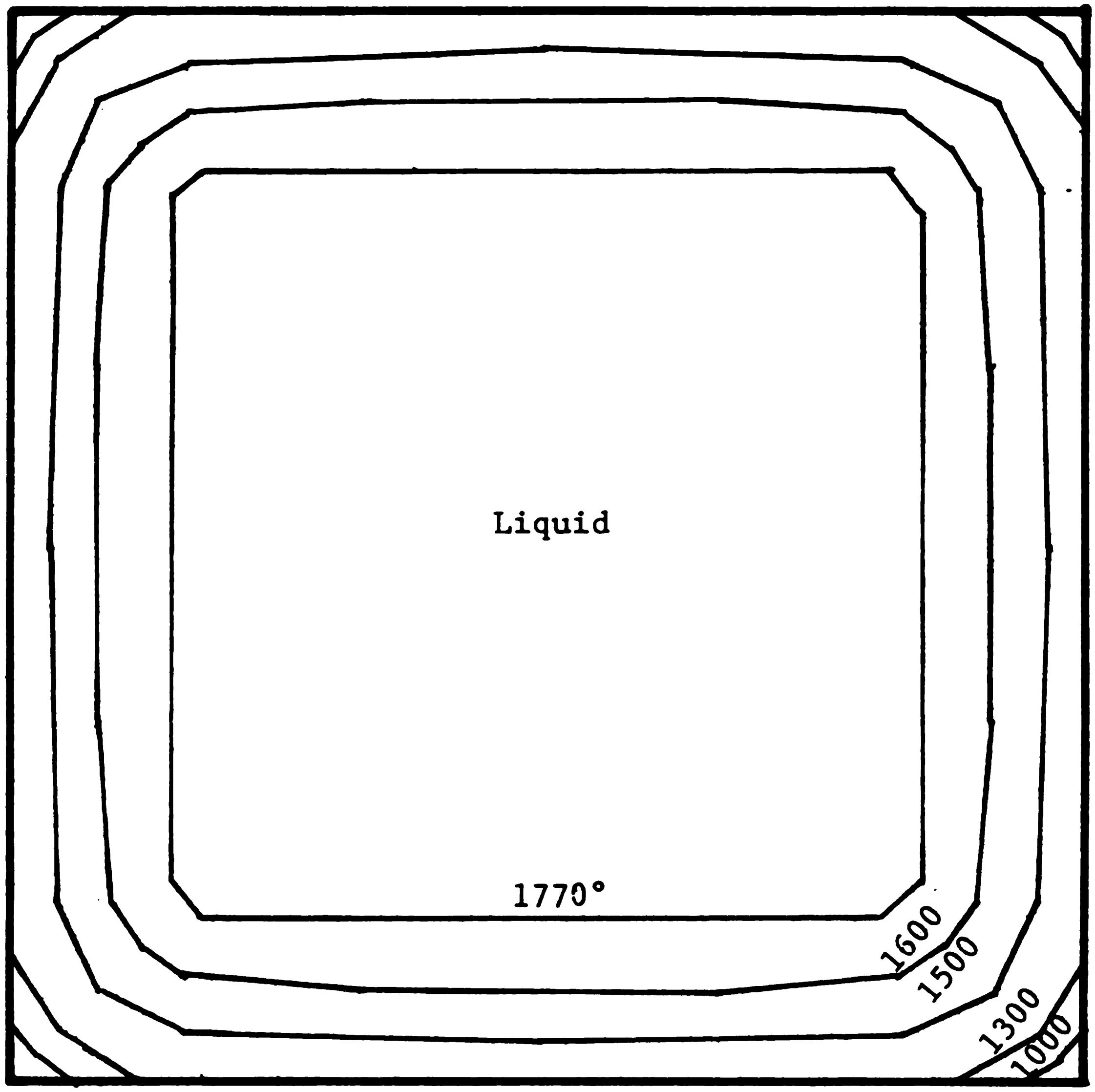

Figure 4-9 Temperature contor lines in x,y plane at 0.5 meters after the mould.

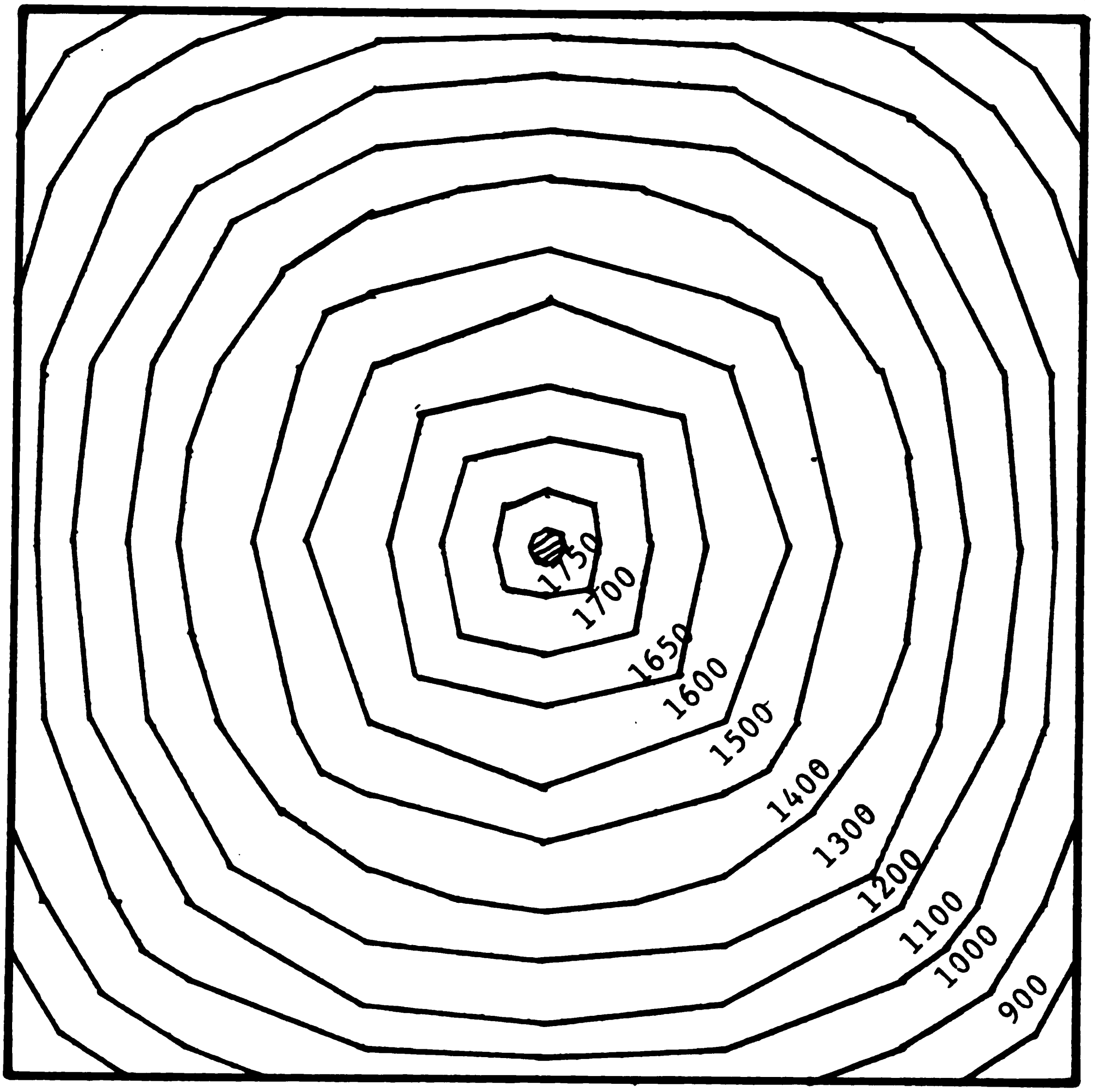

Figure 4-10 Temperature contor lines in x, y plane at just before complete solidification.

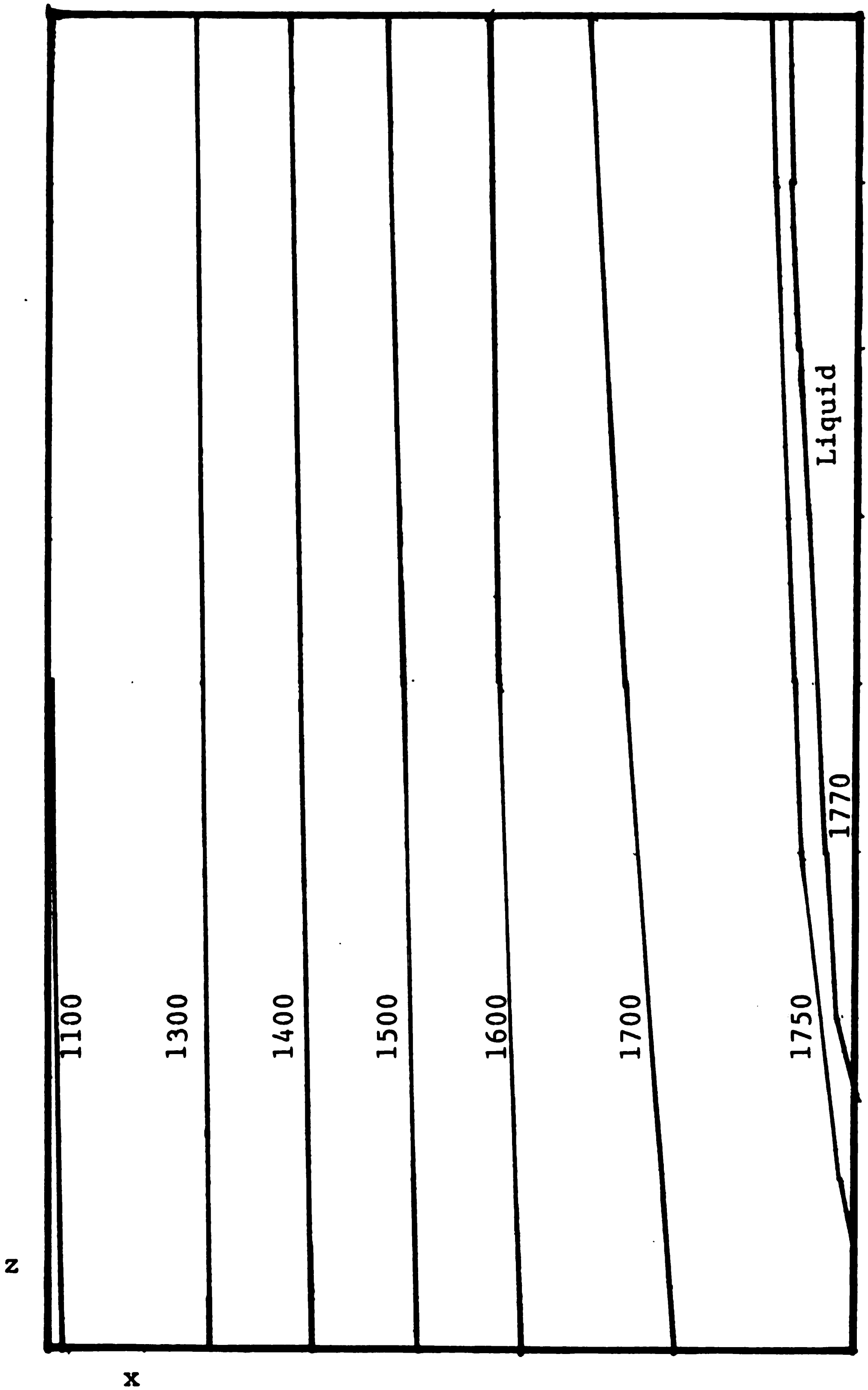

Figure 4-11 Temperature contor lines in x,z plane around complete solidification place.

conditions. Experimental values of shell thickness for the set of conditions assumed in this chapter is not reported anywhere in the literature.

V. COMPUTER PROGRAMMING, NUMERICAL RESULTS, AND STRESS ANALYSIS

5.1 Computer Programming of the Straight Portion

The temperature distribution obtained from the calculations presented in Chapter Three to generate a three-dimensional finite element elasticity program to analyze the stresses within the casting. The program had the following steps: 1) read the number of elements, the number of equations, the band width, the shell thickness, the temperature distribution, and generate the geometry, 2) assign numerical values for the body forces, traction forces and hydrostatic forces, 3) evaluate the element stiffness matrices and the element force vectors, using a local coordinate system and assemble them into a system of equations. Modify the system of equations for known displacements and solve for the nodal displacements, 4) calculate the stress and strain components at several points in each element from displacement values, and 5) evaluate the Von-Mises stress for each element and calculate the ratio of the Von-Mises stress and the element yield stress and output this ratio.

A more detailed discussion of these steps is presented here.

5.1.1 Geometry. The existence of symmetry in the straight portion allowed the analysis to be done using only one-quarter of the total cross-section. The division into the elements is shown in Figure 5-1. A shortage in computer central memory, as was discussed in Chapter Four, required that the straight portion of the casting be solved in several steps. Each step simulated 50 cm of casting in the z direction (the same as in Chapter Four). The solidified shell was assumed to be the only part of the casting which could support a load.

The brick element used in the heat transfer was also used in the stress analysis. The element had twenty nodes and each node had three independent displacements, a component in each coordinate direction. Figure 5-2a shows the cross-section of the ingot and its nodes, when there is an internal liquid. Figure 5-2b shows the grid used after complete solidification had occurred.

5.1.2 Applied Forces and Known Displacements. There are two sets of forces that can act on the ingot, internal forces and boundary forces.

5.1.3 Internal Forces. The body force is the mass of the element which was assumed to be 7.4 g/cm^3 (Grill et al., 1977) acting in the direction of the casting.

Internal surface forces include the ferrostatic pressure which is due to a change in the volume of the liquid under contraction of the surrounding solid shell.

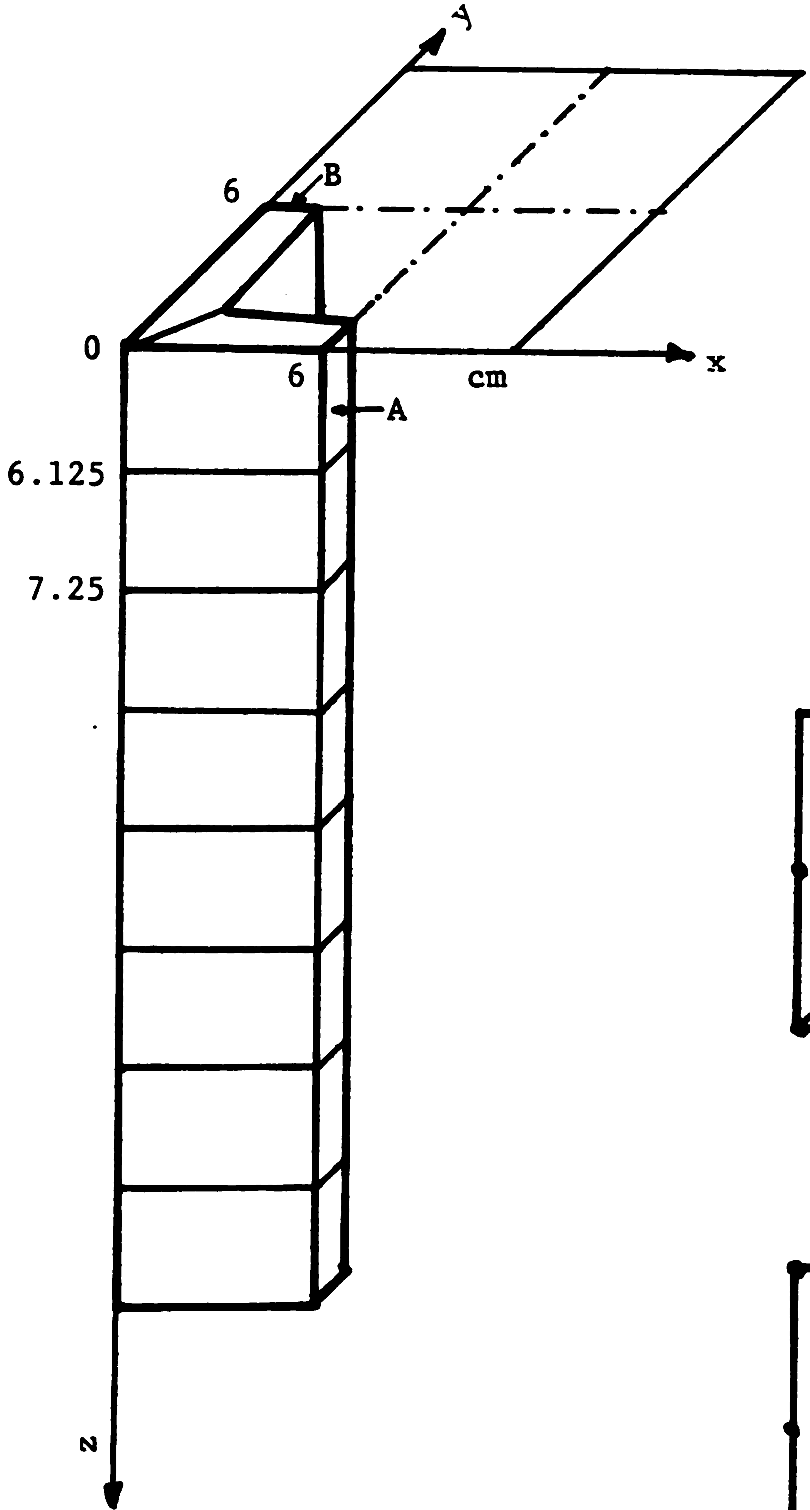

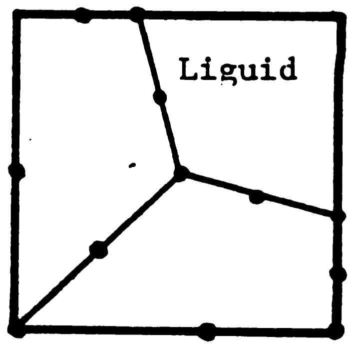

Figure 5-2(a)

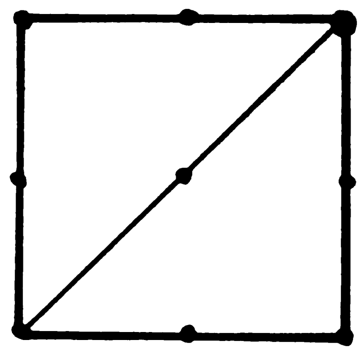

Figure 5-2(b)

Figure 5-1 Division into elements, dimension and location of the coordinate at straight part of casting.

Figure 5-2 Distribution of the nodes at x, y plane (a) before complete solidification, (b) after complete solidification.

An approximation value of 196 N/cm^2 for the ferrostatic pressure was taken from Sonmachi et al. (1979).

5.1.4 External Forces. Friction forces result from the contact of the bulged ingot surface with guidance rolls. Bulging is not large under elastic deformation thus these friction forces were ignored.

A shear force is produced by the pinch rolls. Because the straight sections under analysis were not close to the pinch rolls, the pinch roll loads were assumed to exist as a normal stress applied to the bottom of the section. The value was assumed to be 981 N/cm^2 (Grill et al., 1976).

The displacements on the face indicated by A in Figure 5-1 in the x direction and the displacements on the face denoted by B in the y direction are zero because of symmetry.

The first portion was assumed to have zero displacements in the z direction on the upper face. For the other portions the displacements at the bottom of the last layer would define the displacements for the upper face on the next one.

5.1.5 Element Matrices. Equations 3-9 and 3-10 were used to evaluate the element stiffness matrix and force vector. The material properties which are temperature dependent were calculated at each integration point. The element stiffness matrix and force vector were calculated in a local coordinate system and assembled into a global system of equations. The equations were then modified to incorporate known displacements and solve for unknown nodal displacements.

5.1.6 Stresses and Strains. Once the nodal displacements are known, the strains can be calculated using the strain displacement relationship. The stresses are then calculated using Hooke's law. The isotropic material properties were 0.33 for Poisson's ratio and

$$E = 1.06x10^{7} - 1.01x10^{4}(T-T_{Tr})N/cm^{2}$$

For the elastic modulus (Koster, 1948). In this equation T is the nodal temperature and T_{Tr} the A3 transformation temperature which was assumed to be 870°C.

The yield strain for cast steel was calculated using

$$\varepsilon_{el} = 1.47x10^{-4} - 8.0x10^{-8}xT \quad \text{For } T<1100^{\circ}C$$

$$\varepsilon_{el} = 4.84x10^{-4} - 3.68x10^{-7}xT \quad \text{For } T>1100^{\circ}C$$

(Grill et al., 1977).

The yield stress was calculated by $\sigma_y=\varepsilon_{el}\cdot E$ where σ_y is the yield stress, ε_{el}, σ_y, and E were calculated at the same temperature for any point.

5.2 Von-Mises Yield Stress

The final step was to define the probable regions of crack formation. This was done by calculating the ratio of the Von-Mises stress to the maximum yield stress at the same temperature. The Von-Mises stress is defined as $\sqrt{3J_2}$

where J_2 is the second stress in variants.

$$J_2 = [\tfrac{1}{2}(S_x^2 + S_y^2 + S_z^2) + \tau_{xy}^2 + \tau_{xz}^2 + \tau_{yz}^2]^{\frac{1}{2}}$$

where
$$S_x = \sigma_{xx} - \sigma_m$$
$$S_y = \sigma_{yy} - \sigma_m$$
$$S_z = \sigma_{zz} - \sigma_m$$
$$\sigma_m = \frac{1}{3}(\sigma_{xx} + \sigma_{yy} + \sigma_{zz})$$

All calculations were done in cylindrical coordinates where θ was in the direction of the casting.

The higher the ratio value the more likely the possibility of crack formation.

5.3 Computer Programming of the Curved Part

The program used for the straight sections was modified to calculate the stress ratios in the curved section of the ingot. The changes which were incorporated include the following.

5.3.1 Geometry. Because of the curvature, there were compression and tension stresses, respectively, on the inside and outside of the curve. Thus, it was necessary to analyze one-half of the cross-section. Figure 5-3 shows the cross-section and 5-4 shows the division into elements.

5.3.2 Applied Forces and Known Displacements. In addition to those forces and known displacements which

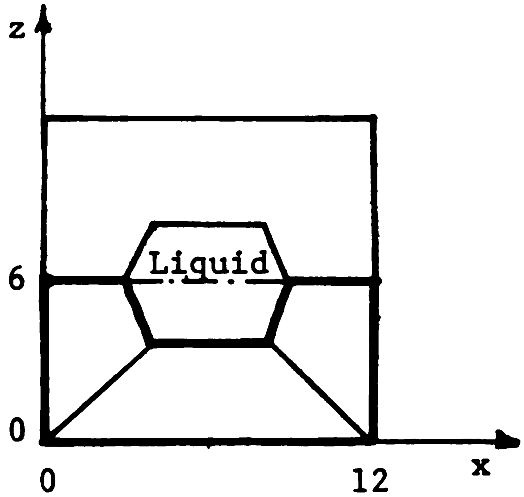

Figure 5-3 Dimension and division into elements in x,y from section of curved portion.

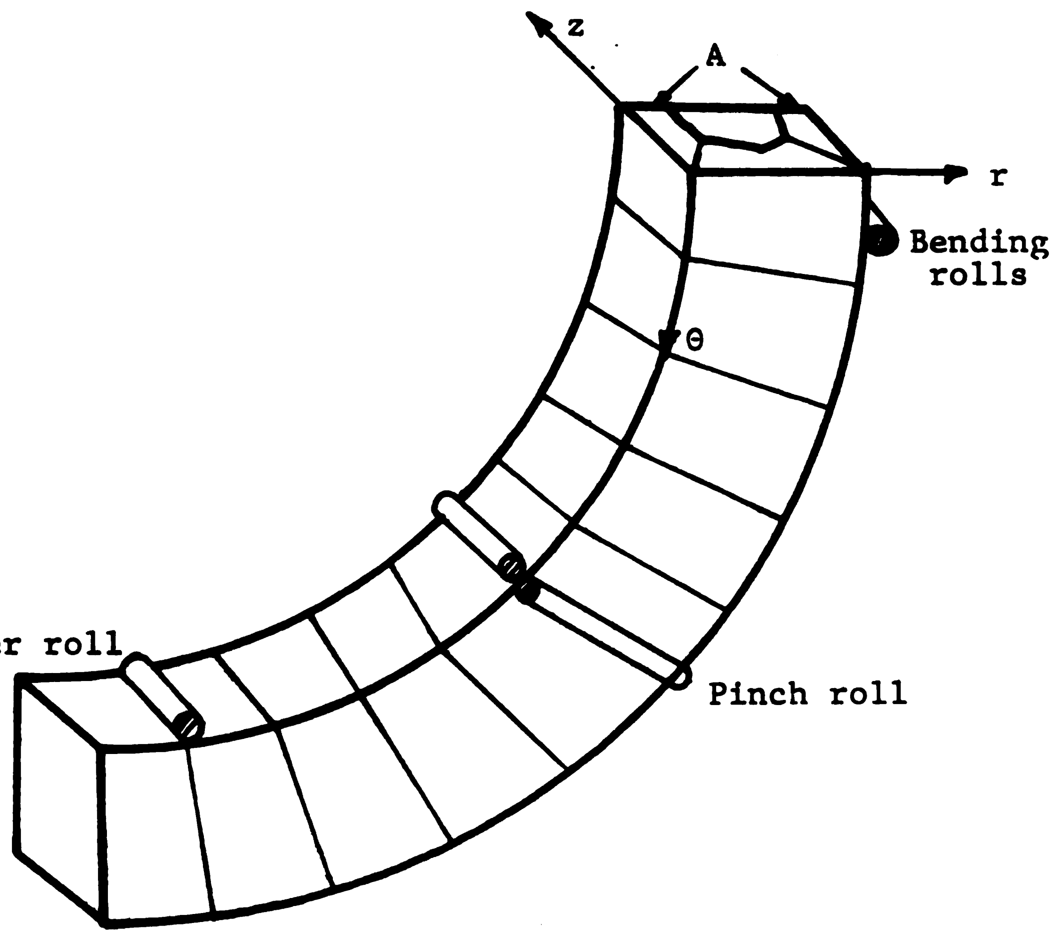

Figure 5-4 Division into the elements along z direction and location of the cylindrical coordinates, Bending roll, pinch roll, and straightner roll in curved portion.

existed in the straight section, there are additional forces. These are:

<u>Bending Forces</u>: Figure 5-4 shows the bending rolls which forces the ingot into the curve shape. The magnitude of these forces are dependent on the location of the bending rolls and the radius of the curvature. The assumption of ten layers of elements in the curved portion of the ingot regardless of the total length of the curve leads to a set of known radial displacements located at 4.5 degree increments in the Θ direction due to the bending forces, while $\Theta=0$ was at the beginning of the curved portion. These known displacements were in the direction of the radius of the curvature toward the center and calculated by

$$\Delta R = R - R \cos (4.5^{\circ})$$

where R is the displacement due to the bending force and R is the radius of the curvature.

The <u>body force</u> was divided into two components. One component was in the direction of the radius of the curvature and equal to F Sin(θ). The other was in the direction of the casting, Θ and equal to F Cos (Θ) where F is the body force in the straight portion of the ingot.

The <u>pinch rolls</u> which produce the ingot movement in the direction of the casting applied a set of forces to the casting. These were assumed to be at $\Theta=45^{\circ}$ location and acting on each side of the ingot. The pinch rolls were assumed to develop shear forces at applied nodes by the value of 9800 N per node.

The straightener forces forced the casting to move horizontally after $\Theta=90^{\circ}$. These forces were assumed to be located at $\theta=85.5^{\circ}$ and caused displacements opposite to the radius. These displacements were calculated by $\Delta R = R - R\ \mathrm{Cos}(4.5)$.

The mass of the ingot after the straightener and before the cut off point resists free movement of the ingot under the applied forces. This opposing force, which is friction, can be modeled as a set of springs which are attached on the ingot cross-section beyond the straightener. The spring constant used was 7.06(E+6)N/cm. These stiffnesses were added to the diagonal of the global stiffness matrix.

Because of symmetry, the displacements at the surface denoted by A in Figure 5-3a are zero in the z direction.

The surface displacements of the ingot at the outside of the curve in contact with the guidance rollers in the direction of the radius of the curvature at the location of the rollers are zero.

5.3.3 Element Stiffness Matrix, Curved Elements. To derive the element stiffness matrix and element force vector, equations 3-9 and 3-10 were written in cylindrical coordinates. In order to analyze the curved portion, the determining Jacobian transformation from Cartesion to cylindrical coordinates is r, the radius of the curvature at the integration point.

For example, the volume in Cartesian coordinates is

$$dV = dxdydz$$

at the cylindrical coordinates

$$dV = |r|dxdydz$$

and at the natural coordinates

$$dV = |r| \; |\det[J]| \; d\xi d\eta d\zeta$$

where [J] is the Jacobian transformation to natural coordinates.

5.4 Result

5.4.1 General. In order to study the possibility of crack formation, the stress distribution in the solid shell, and the value of the ratio of Von-Mises stress to the minimum stress required for cracking must be known as a function of temperature. Although there is little data on which to base this criterion, strength measurements made be Adams (1971) and Hall (1936) can be used as a rough guide. They found that for temperatures increasing above 1525°K the strength of carbon steels decreases rapidly and for temperatures above 1595°K the steel is very brittle. Based on this information special care must be taken whenever the ingot temperature is above 1525°K. The stress ratio must be kept as low as possible in regions having these temperatures.

Considering the above information and using the program for the straight and curved portions of the ingot, the results of the stress analyses are shown in Figures 5-5 through 5-20. Figure 5-5 gives the key for understanding Figures 5-6 through 5-20. In these fourteen figures the stress ratios are plotted for various distances beyound the mould for different sets of conditions,

5.4.2 Straight Portion. The casting was analyzed from the exit of the mould to the straightener rolls on the casting. Any point with a high stress ratio has a greater chance of crack formation. Of all the points shown, the highest stress ratio occurs at the bending rolls. The results can be interpreted as follows. The high stress ratio in the region zero to twenty centimeters after the mould is observed in section B rather than section A and C. Between zero and twenty centimeters below the the mould the temperature distribution has an increase in surface temperature of about $170^{\circ}K$ in section B. The increase in temperature here is due to a change of the heat transfer coefficient from the mould to spray cooling water. This rapid change in the ingot surface temperature causes the high stress ratio. It has been reported that cracks occur in these locations and were observed experimentally by Grill et al. (1976).

The pinch rolls would cause high surface stresses and the possibility of surface cracks. The complete solidification leads to a sharp drop in the center temperature which may cause center line cracks. The stresses due to pinch rolls and complete solidification were assumed in the curved portion. There are not other significant places with high stress ratios to cause a crack in the straight part.

5.4.3 Curved Portion. The location of the bending rolls was varied from 50 cm to 400 cm below the mould. The radius of curvature was taken from 76.4 cm to 343.8cm. The first consideration was the location of the bending rolls. Comparing the different location of the bending rolls indicated that having them far from the mould caused a higher stress ratio at the location of the bending rolls. The reason is that the mass of the casting which has to be dislocated by the bending rolls will increase by having those rolls far below the mould. On the other hand, the pinch rolls and straighteners cause the additional possibility of half way cracks when the bending rolls are too close to the mould. The pinch rolls which were assumed to be located between the bending rolls and straightener rolls seem more likely to cause the surface cracks. These surface cracks occurred more if the curved part of the ingot was too close to the mould rather than having the curve far below the mould.

The second consideration was the radius of curvature. Looking at Figures 5-6 through 5-20 shows that a higher radius decreased the stress ratio at the location of the bending rolls. On the other hand, lower radius of curvature caused more displacement in the mass of casting in the radial direction at the location of the bending rolls. In addition, the high radius decreases the risk of surface crack at the location of the bending rolls.

Finally, if the radius and the location of the curved parts are considered, the overall risk of forming cracks would be lowest if the curve is located after complete solidification or as close to the mould as possible. In either case the radius must be as large as possible. Any other condition will increase the chance of crack formation. All these results were interpreted from Figures 5-6 through 5-20.

Due to uncertainty in the value of the applied forces, any increase in the stress ratios may be considered as an important one because the increase in the value of applied forces will increase those stress ratios and make their corresponding location a good place to form the cracks. So, ignoring whether the stress ratios are realistic or not because of the force values which were used, one can compare the results to make a certain conclusion.

Overall from the economic point of view it seems that if the curve started immediately after the beginning of solidification there would be no need for having a very high shelter and the additional expensive material to support the casting installation. Also, the supporting rolls may support less load and, therefore, have a longer lifetime (Nozaki et al., 1977).

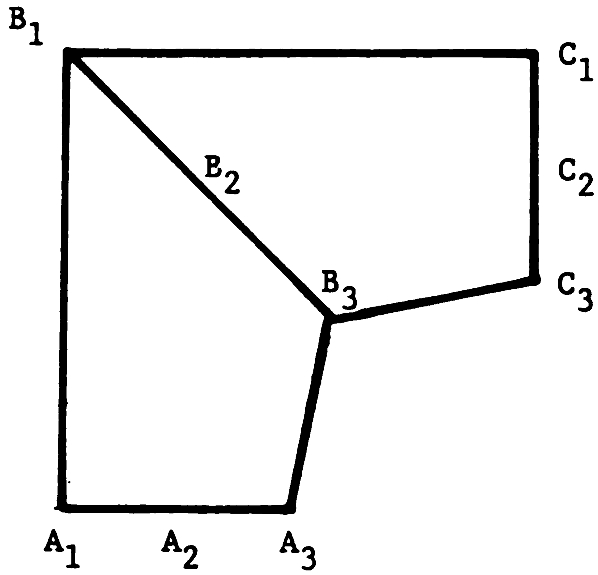

——————— index 1 near the casting surface

\- - - - - - index 2 between casting surface and solidification front

— — — — — — index 3 near solidification front

A the surface which bending force applied on it

B section from corner to the center of casting

C location in neutral axis

Figure 5-5 Key figure for Figures 5-6 through 5-20.

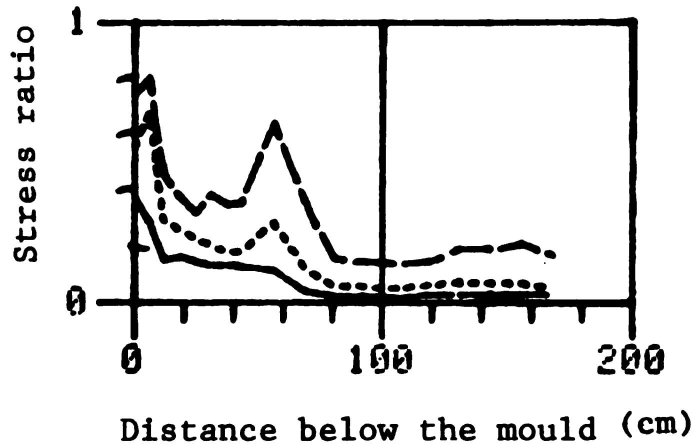

B

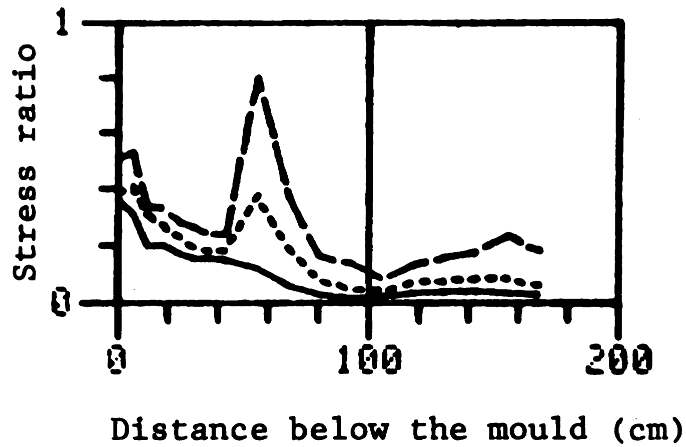

C

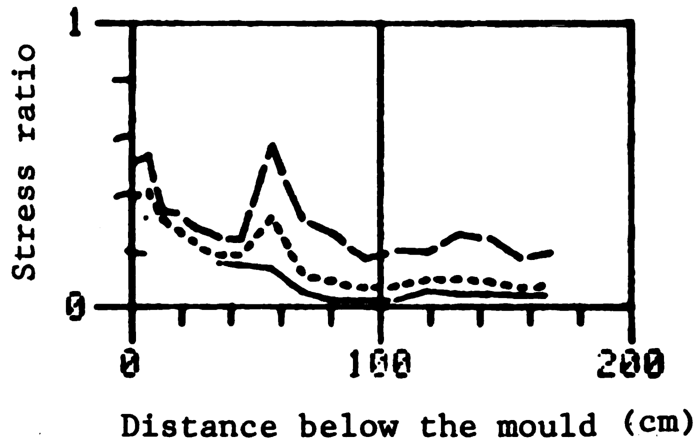

A

Radius of curved portion = 76.4
Location of bending rolls = 50cm
after the mould.

Figure 5-6 Stress ratio along the z direction

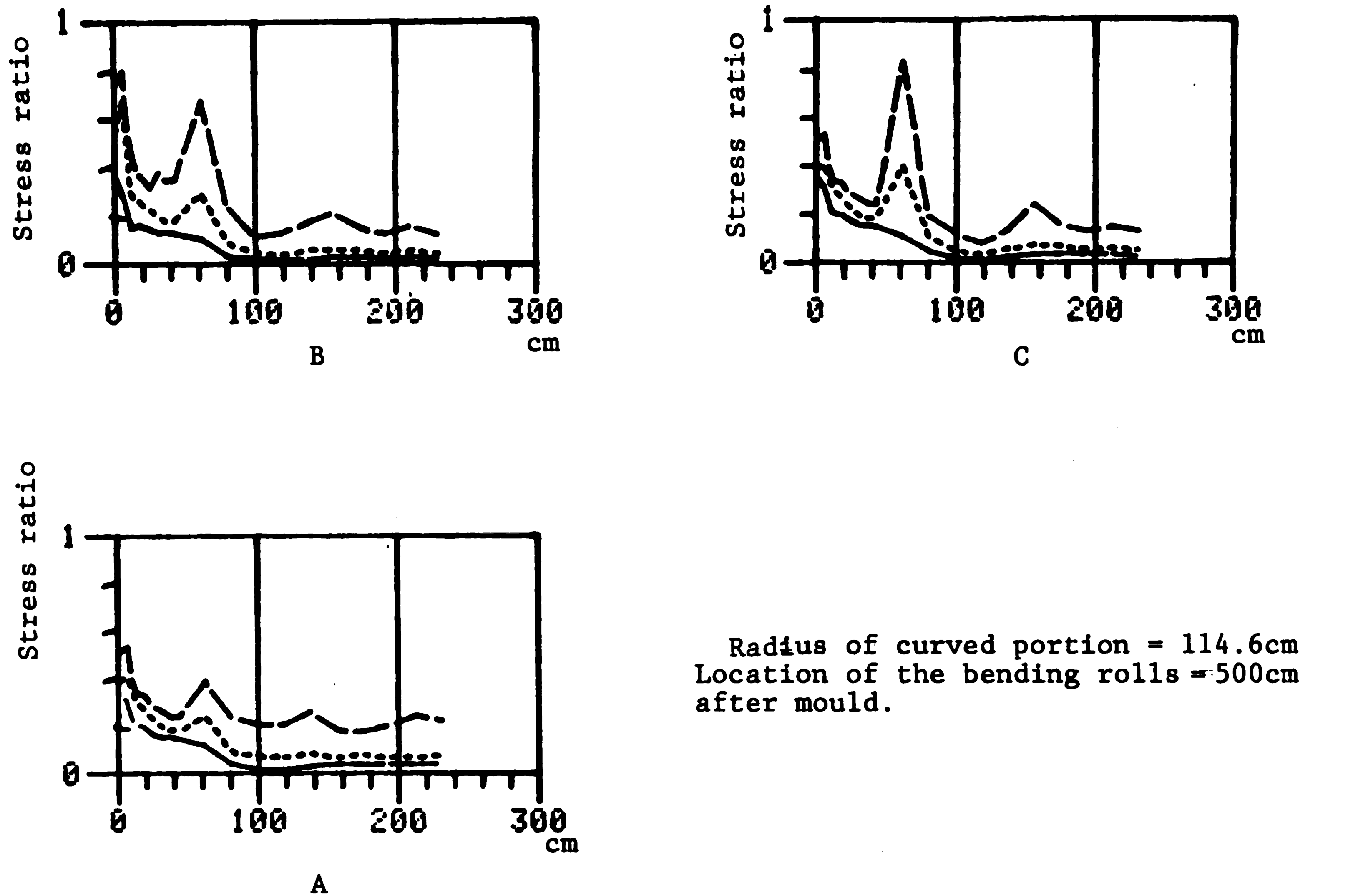

Radius of curved portion = 114.6cm
Location of the bending rolls = 500cm
after mould.

Figure 5-7 Stress ratio along z direction.

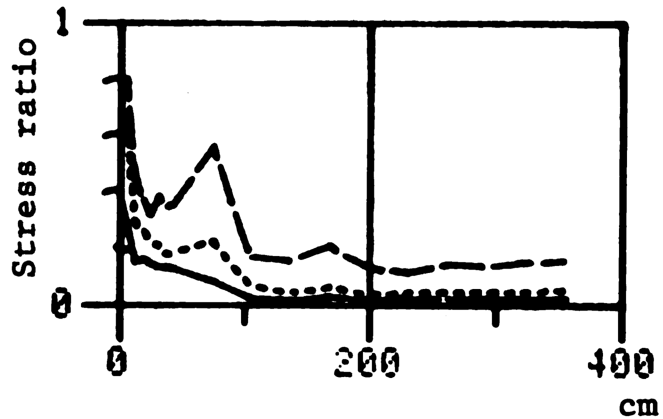

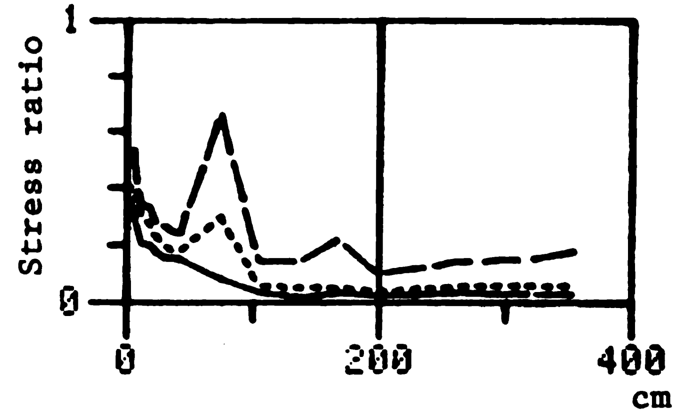

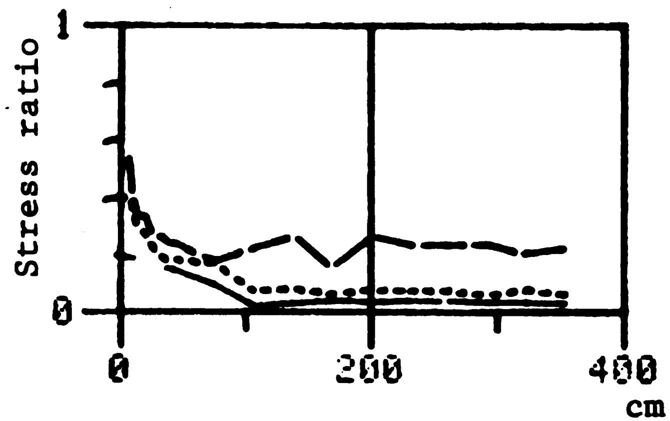

Radius of curved portion = 191cm
Location of the bending
rolls = 50cm after the mould.

Figure 5-8 Stress ratio along z direction.

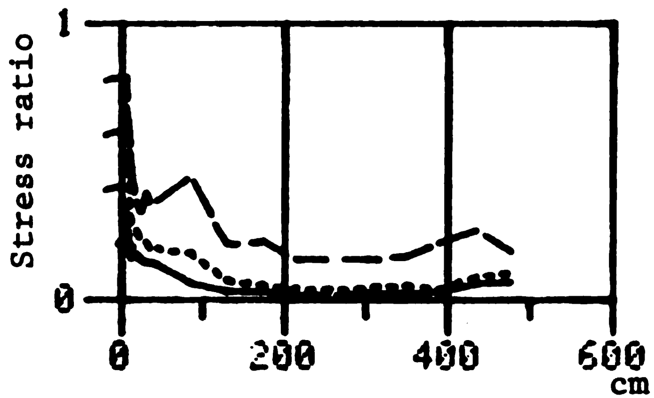

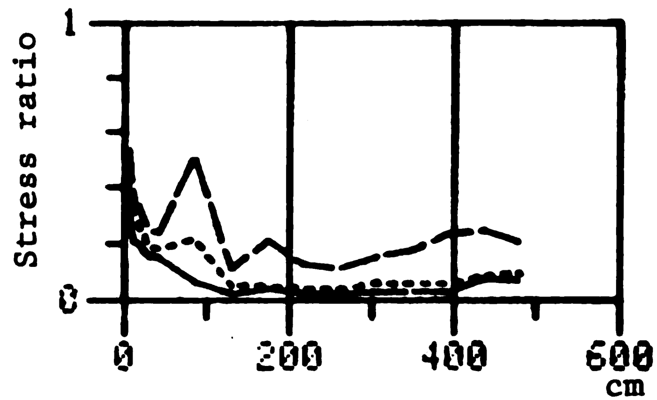

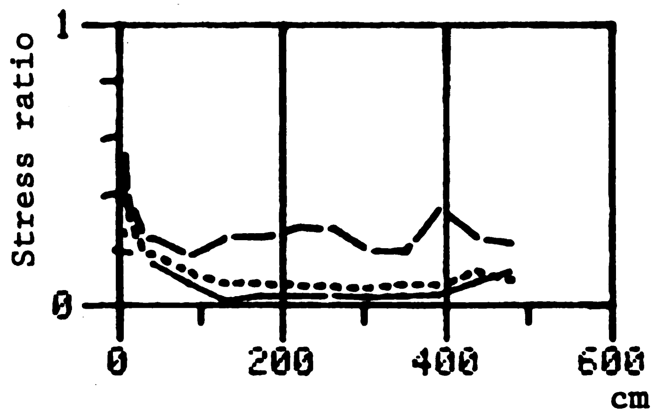

Radius of curved portion = 267.4cm
Location of the bending
rolls = 50cm after the mould

Figure 5-9 Stress ratio along z direction.

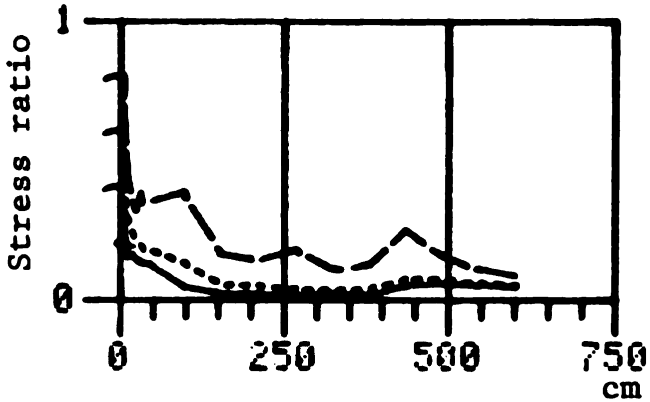

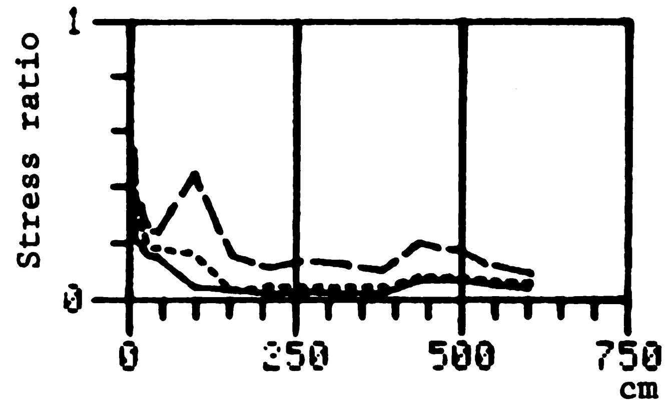

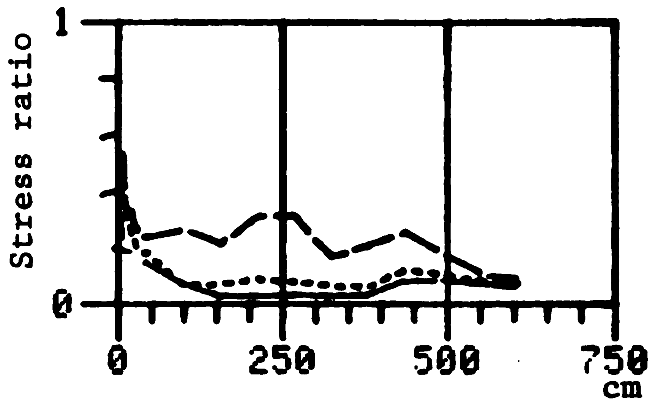

Radius of curved portion = 343.8cm
Location of the bending rolls = 50cm
after the mould.

Figure 5-10 Stress ratio along z direction.

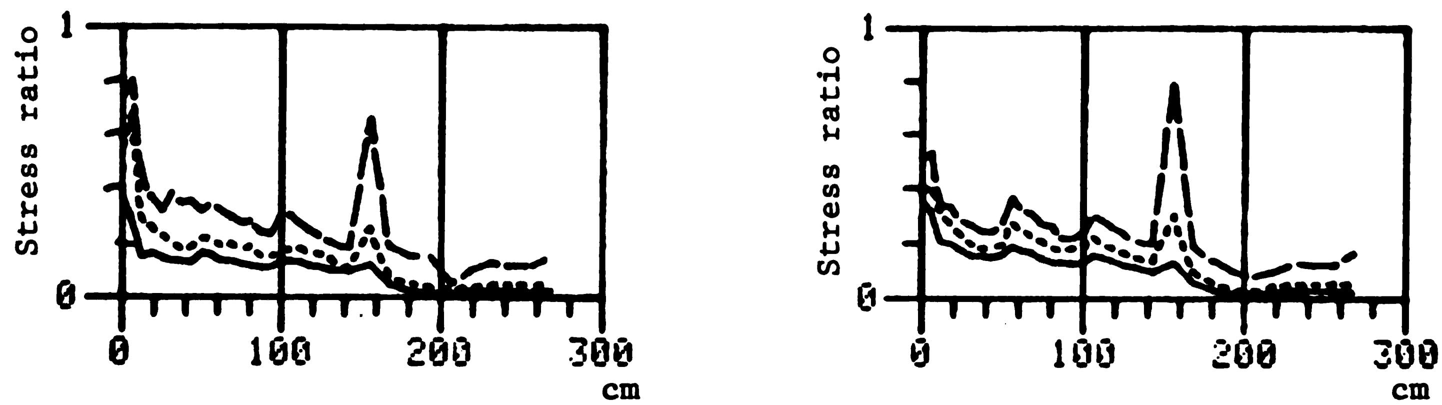

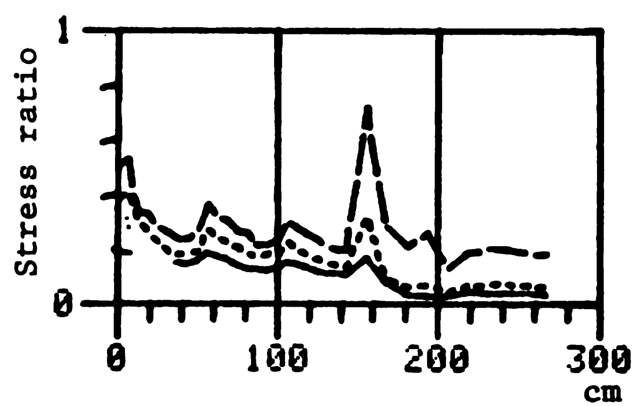

Radius of curved portion = 76.4cm
Location of the bending rolls = 150cm
after the mould.

Figure 5-11 Stress ratio along z direction.

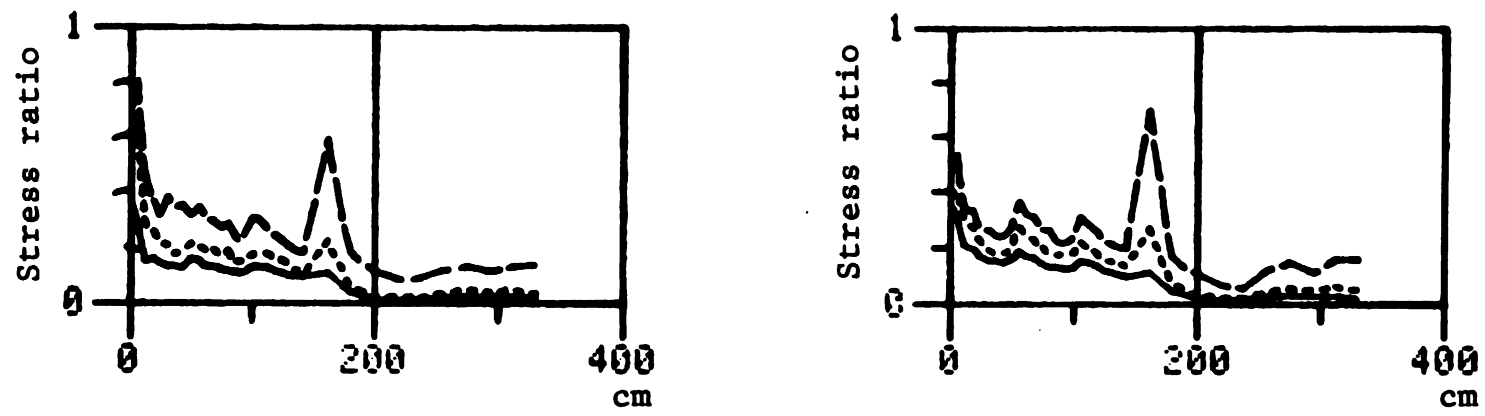

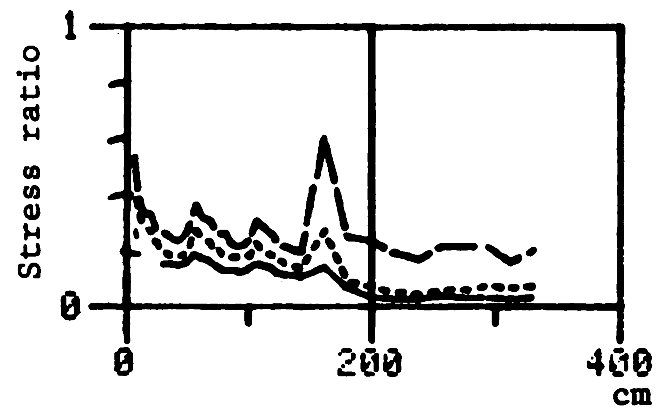

Radius of curved portion = 114.6cm
Location of the bending rolls = 150cm
after the mould.

Figure 5-12 Stress ratio along z direction.

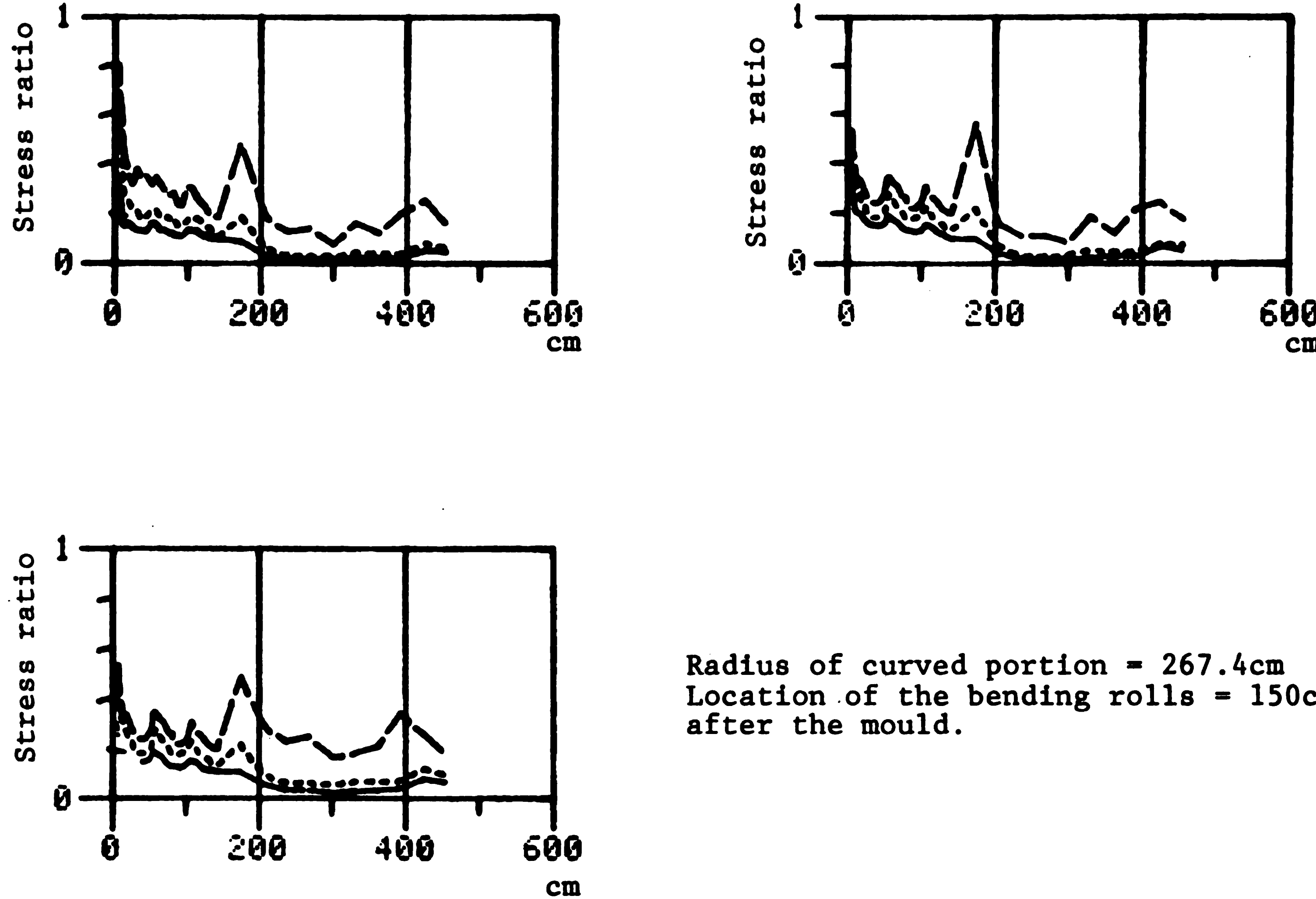

Radius of curved portion = 267.4cm
Location of the bending rolls = 150cm
after the mould.

Figure 5-13 Stress ratio along z direction.

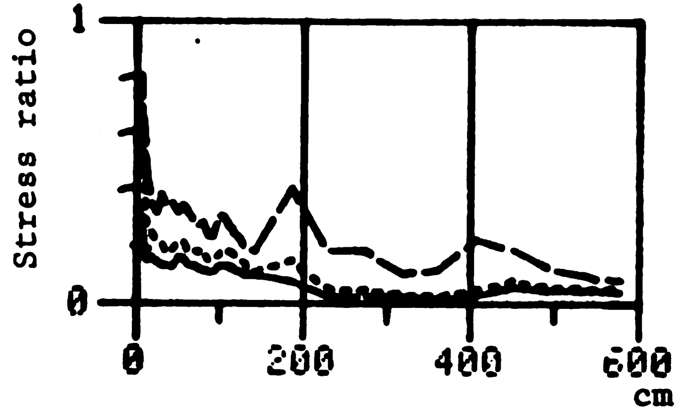

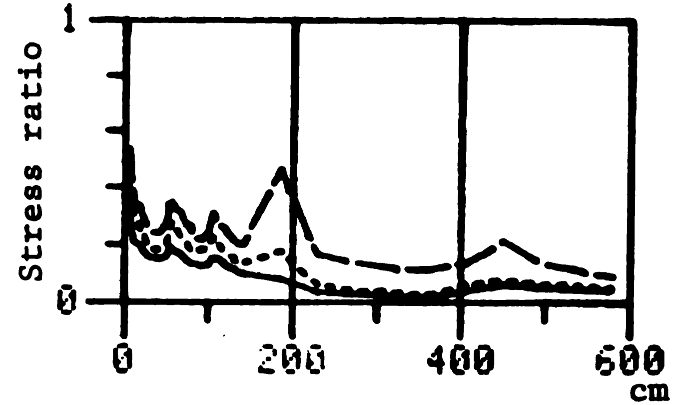

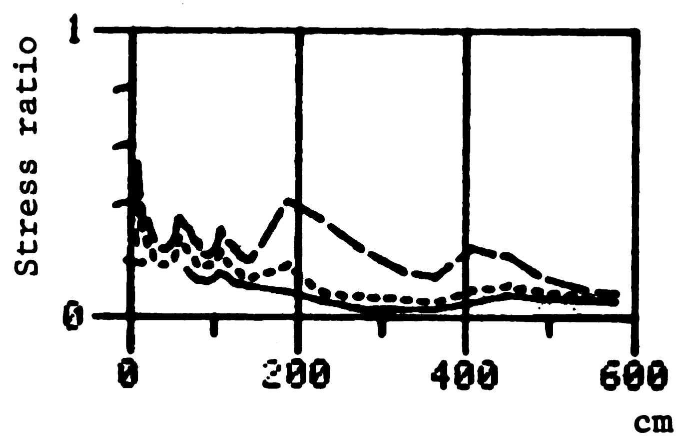

Radius of curved portion = 267.4cm
Location of the bending rolls =150cm
after the mould.

Figure 5-14 Stress ratio along z direction.

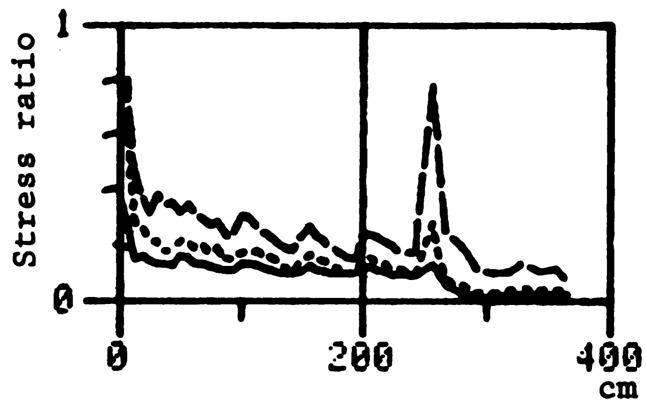

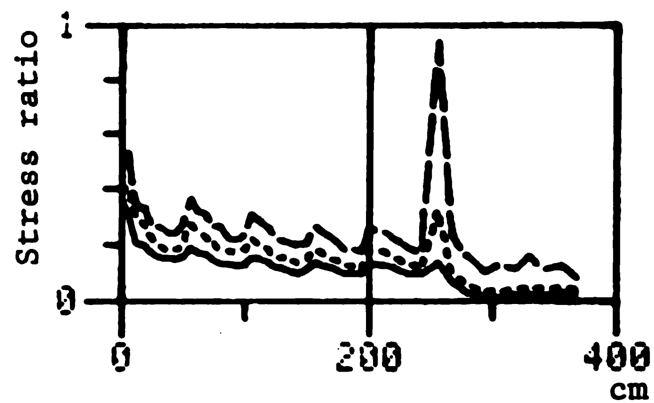

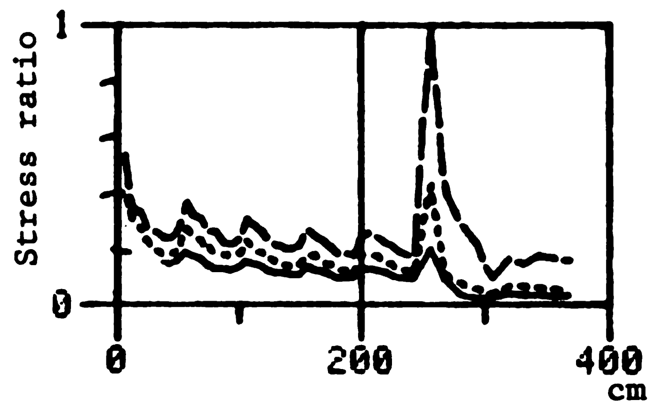

Radius of curved portion = 76.4cm
Location of the bending rolls = 250cm after the mould.

Figure 5-15 Stress ratio along z direction.

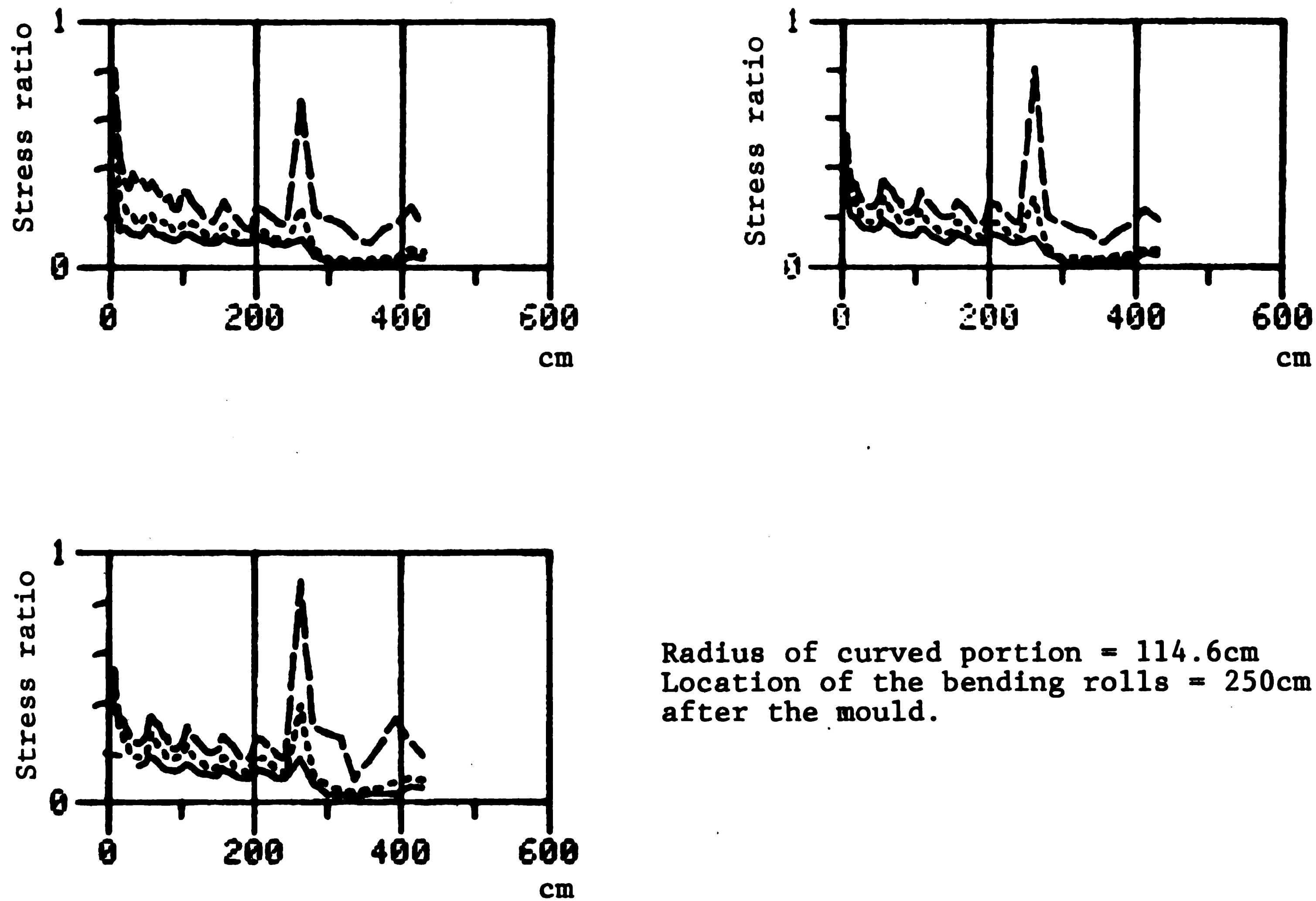

Radius of curved portion = 114.6cm
Location of the bending rolls = 250cm
after the mould.

Figure 5-16 Stress ratio along z direction.

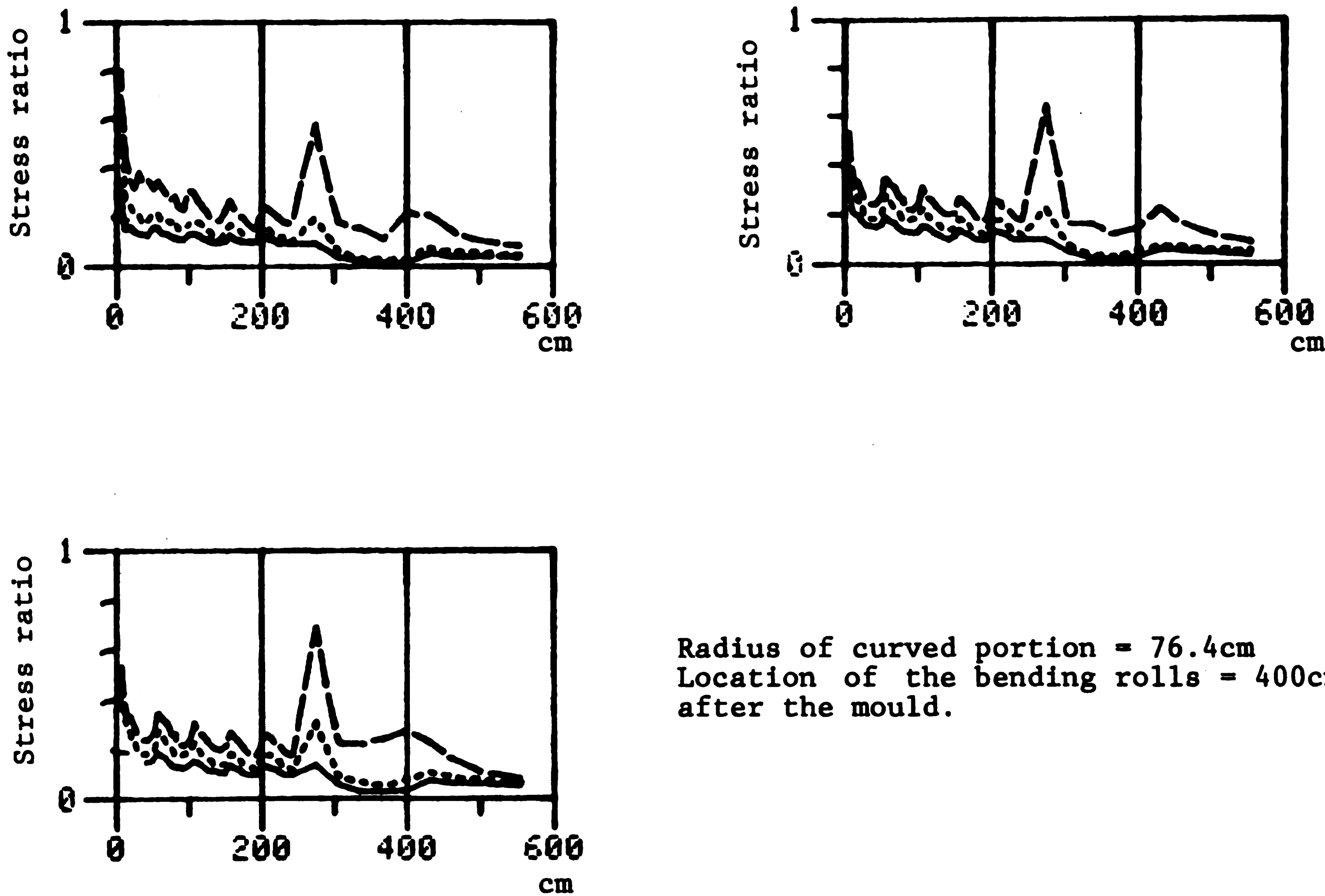

Radius of curved portion = 76.4cm
Location of the bending rolls = 400cm
after the mould.

Figure 5-17 Stress ratio along z direction.

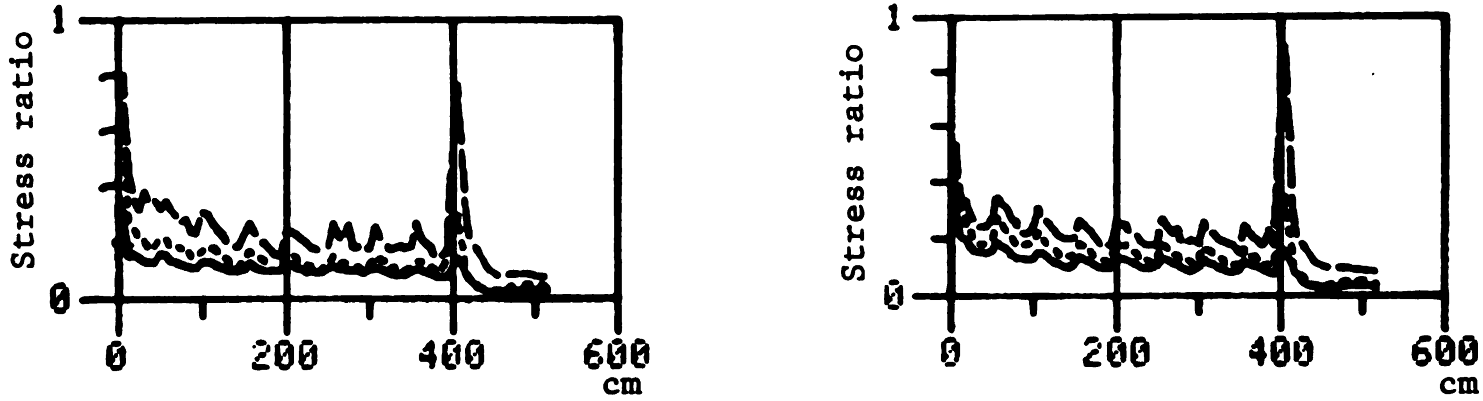

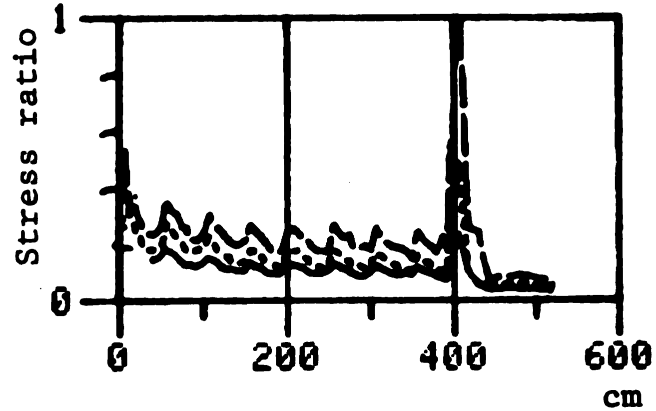

Radius of curved portion = 76.4cm
Location of the bending rolls = 400cm
after the mould.

Figure 5-18 Stress ratio along z direction.

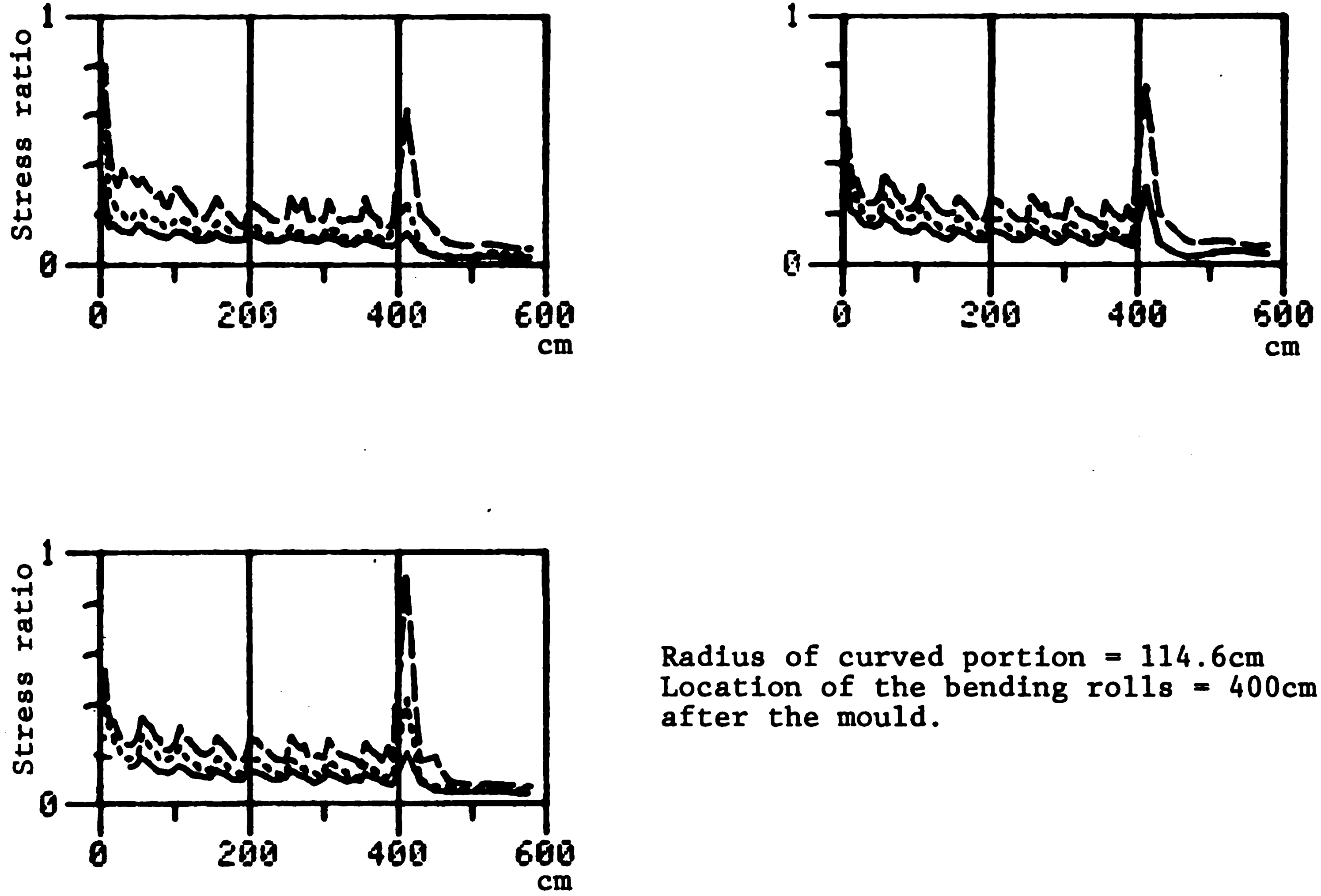

Figure 5-19 Stress ratio along z direction.

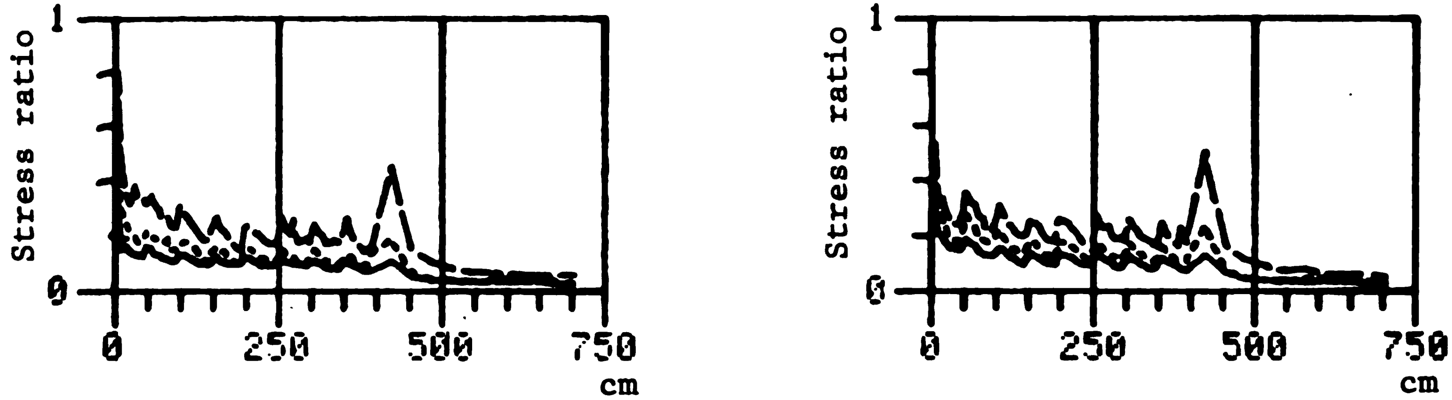

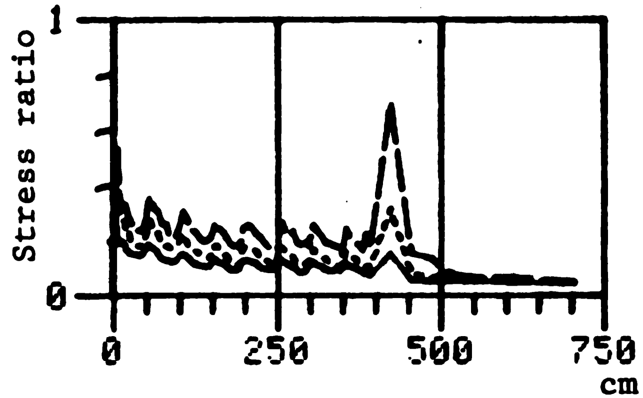

Radius of curved portion = 191cm
Location of the bending rolls = 400cm
after the mould.

Figure 5-20 Stress ratio along z direction.

VI. CONCLUSIONS

This study is the beginning of the application of the three-dimensional finite element technique to analyze a continuous casting. The numerical model developed was capable of calculating a good approximation of the temperature distribution in a continuous casting and, a rough approximation of the stress distribution resulting from temperature gradients, and internal and external forces. Due to the lack of information on the mechanical properties data for steel at high temperature the stress ratios obtained have a limited value.

Based on the numerical results obtained, it was concluded that: a) the three-dimensional finite element method is applicable to the analysis of the cooling process in a continuous casting and gives a reasonable temperature distribution for the ingot; b) the results obtained in this study were an improvement over those previously reported. The ingot surface temperature at the exit of the mould has been measured to be 1330^{O}K, a two-dimensional finite difference analysis gave 1407^{O}K (Lait et al.,1974). and a two-dimensional axisymmetric finite element analysis gave 1483^{O}K (Mathew, 1974). A temperature of 1350^{O}K was calculated in this study; c) the stress analysis, which incorporated many assumptions, shows that the most logical place to locate the curve region of the casting was as close as possible to the mould. The radius should be made as large as possible to reduce crack formation; and d) an approximation method of analysis which divided the casting into segments gave temperature results which agreed well with an analysis which included the entire length.

BIBLIOGRAPHY

BIBLIOGRAPHY

1. Adams, C.J., Partial Annealing of Low Carbon Steel Strip, AIME Open Hearth Proc., pp. 290, 1971.

2. Brimacombe, J.K., and Weinberg F., Continuous Casting of Steel, Journal of the Iron and Steel Institute, pp. 24, 1973.

3. Campagna A.J., Heat Flow in Solidification of Alloys, Ph.D. Dissertation M.I.T., 1970.

4. Denhartog, H.W., Rabenberh, J.M., and Willemse J., Application of a Mathematical Model in the Study of the Ingot Solidification Process, Iron Making and Steel Making, pp 134, 1975.

5. Fischer, G.A., Solidification and Soundness Prediction for Large Steel Ingots, Proceedings ASTM, pp. 1137, 1970.

6. Grill, A., Brimacombe, J.K., and Weinberg, F., Mathematical Analysis of Stress in Continuous Casting, Iron Making and Steel Making, pp. 38, 1976.

7. Grill, A., and Brimacombe, J.K., Influence of Carbon Content on Rate of Heat Extraction in the Mould of a Continuous Casting Machine, Iron Making and Steel Making, pp. 76, 1976.

8. Grill, A., Sorimachi, K., and Brimacombe, J.K., Heat Flow, Gap Formation, and Break-outs in the Continuous Casting of Steel Slabs, Metallurgical Transaction, pp. 177, 1976

9. Gautier, J.J., Morillon, J., and Dumont-Fillon J., Mathematical Study of the Continuous Casting of Steel, Journal of the Iron and Steel Institure, pp. 1053, 1970.

10. Hall, H.F., Second Report of Steel Casting Research Committee, Iron and Steel Institute, London, pp. 65, 1936.

11. Hills, A.W.D., Simplified Theoretical Treatment for The Transfer of Heat in Continuous Casting Machine Moulds, Journal of the Iron and Steel Institute, pp. 18, 1965.

12. Koler, A.I., Thomas, J.D. and Tzavaras, A.A., Computation of Heat of Fusion in a Mathematical Model for Large Steel Cast Shapes, Cast Metals Research Journal, pp. 156, 1973.

13. Koster, W., Zeitschrift Fur Metallkunde, pp. 10, 1948.

14. Lait, J.E., Brimacombe, J.K., and Weinberg, F., Pool Profile, Liquid Mixing and Cast Structure in Steel, Continuously Cast in Curved Moulds, Iron Making and Steel Making, pp. 35, 1974.

15. Lait, J.E., Brimacombe, J.K., and Weinberg, F., Mathematical Modelling of Heat Flow in the Continuous Casting of Steel, Iron Making and Steel Making, pp. 90, 1974.

16. Lankford, W.T., Jr., Some Considerations of Strength and Ductility in the Continuous Casting Process, Metallurgical Transactions, pp. 1331, 1972.

17. Marrone, R.E., Wilkes J.O., and Pehlke, R.D., Numerical Simulation of Solidification, AFS Cast Metals Research Journal, pp.184, 1970.

18. Mathew, J. and Brody, H.D., Analysis of Heat Transfer in Continuous Casting Using a Finite Element Method, Int. Conf. on Computer Simulation for Materials Applications Proc., pp. 1138, 1976.

19. Mizikar, E.A., Spray Cooling Investigation for Continuous Casting of Billets and Blooms, Iron and Steel Engines, pp. 53, 1970

20. Mizikar E.A., Mathematical Heat Transfer Model for Solidification of Continuous Cast Steel Slabs, Transactions of the Metallurgical Society of AIME, pp. 1747, 1967.

21. Morton, S.K. and Weinberg, F., Continuous Casting of Steel, Journal of the Iron and Steel Institute, pp. 13, 1973.

22. Nozaki, T., Mori, T., and Kamahara, M., Characteristics of the "Walking-bar" Type Slab Caster, Iron Making and Steel Making, pp. 355, 1977.

23. Raychauphuri, B.C., Computer Prediction of Temperature Profiles and Thermal Stress in Solidification of Metals, Mechanical Engineering Bulletin, pp. 51, 1977.

24. Richards, J.H., U.S. Steel Corp's First Ingot-free Electric Arc Furnace Steel Melting Shop, Iron and Steel Engineer, pp. 41, 1971.

25. Rosenthal, D., The Theory of Moving Sources of Heat and its Application to Metal Treatments, Transaction of the A.S.M.E., pp. 849, 1946.

26. Savage, J. and Pritchard, W.H., The Problem of Rupture of the Billet in the Continuous Casting of Steel, Journal of the Iron and Steel Institute, pp.269, 1954.

27. Schmidt, L. and Fredrikson, H., Formation of Macrosegregation and Center Line Cracks in Continuously Cast Steel, Ironmaking and Steelmaking, pp. 61, 1975.

28. Segerlind, L.J., Applied Finite Element Analysis, Published by John Welley & Sons, Inc., 1976.

29. Sorimachi, K. and Brimacombe,J.K., Improvements in Mathematical Modelling of Stresses in Continuous Casting of Steel, Ironmaking and Steelmaking, pp. 240, 1977.

30. Nusui, G. and Chihara, K., Temperature Calculation in Solidifying and Cooling Process of Ingot, Nippon Technical Report Overseas, 1967.

31. Zienkiewicz, O.C., The Finite Element Method, McGraw-Hill Publications, 3rd ed., 1978.